Cell Reports
Medicine

Article

Optimal target saturation of ligand-blocking anti-GITR antibody IBI37G5 dictates FcγR-independent GITR agonism and antitumor activity

Graphical abstract

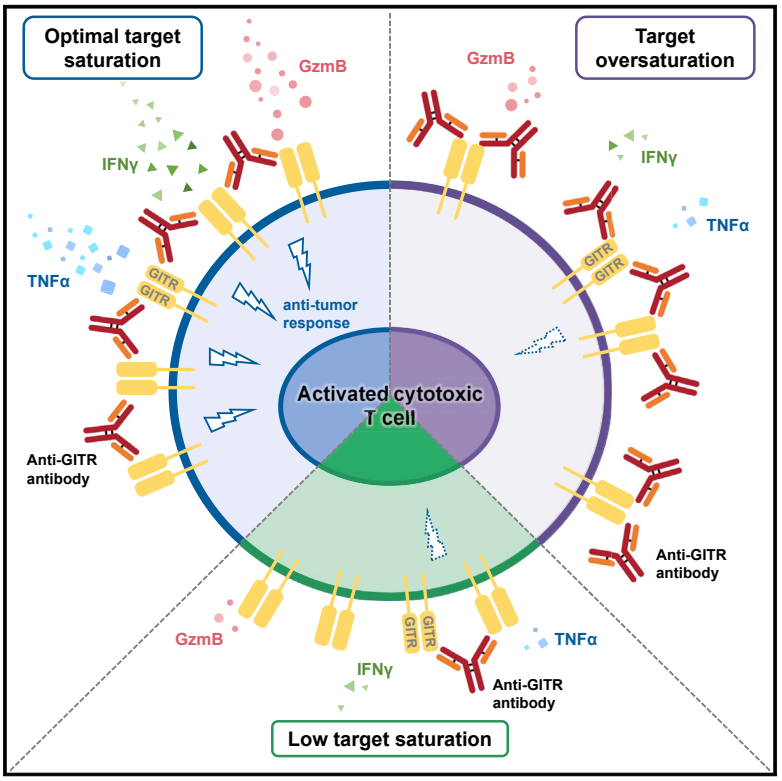

Highlights

- Activated/exhausted tumor-infiltrating CD8$^+$ T cells co-express PD1 and GITR
- Anti-GITR antibody IBI37G5 shows FcγRs-independent agonism and antitumor effect
- IBI37G5 synergizes with anti-PD1 antibody to control established murine tumors
- IBI37G5 exhibits best antitumor efficacy at doses near-saturating target receptors

Authors

Huisi Liu, Weiwei Wu, Gangyu Sun, ..., Wenqing Xu, Zhizhi Wang, Kaijie He

Correspondence

wangzhzh@shanghaitech.edu.cn (Z.W.), kaijie.he@innoventbio.com (K.H.)

In brief

Determining the optimal *in vivo* efficacious doses is essential for the success of anti-GITR antibody development. Liu et al. propose a dose-finding strategy by monitoring the target saturation levels of GITR receptors to predict antitumor efficacy. This finding also has implications for therapeutic antibodies targeting other co-stimulatory receptors.

Liu et al., 2022, Cell Reports Medicine *3*, 100660
June 21, 2022
https://doi.org/10.1016/j.xcrm.2022.100660

CellPress

Cell Reports Medicine

CellPress
OPEN ACCESS

Article

Optimal target saturation of ligand-blocking anti-GITR antibody IBI37G5 dictates FcγR-independent GITR agonism and antitumor activity

Huisi Liu,[1,5] Weiwei Wu,[2,5] Gangyu Sun,[3,5] Tiongsun Chia,[1,5] Lei Cao,[2] Xiaodan Liu,[1] Jian Guan,[1] Fenggen Fu,[4] Ying Yao,[2] Zhihai Wu,[4] Shuaixiang Zhou,[4] Jie Wang,[2] Jia Lu,[2] Zhihui Kuang,[2] Min Wu,[2] Luan He,[1] Zhiyuan Shao,[4] Dongdong Wu,[2] Bingliang Chen,[2] Wenqing Xu,[3] Zhizhi Wang,[3,*] and Kaijie He[1,6,*]

[1]Department of Immunology, Innovent Guoqing Academy, Innovent Biologics (Suzhou) Co., Ltd., Suzhou, China
[2]Department of Pharmacology and Preclinical Studies, Innovent Guoqing Academy, Innovent Biologics (Suzhou) Co., Ltd., Suzhou, China
[3]School of Life Science and Technology, ShanghaiTech University, Shanghai, China
[4]Department of Antibody Discovery and Protein Engineering, Guoqing Academy, Innovent Biologics (Suzhou) Co., Ltd., Suzhou, China
[5]These authors contributed equally
[6]Lead contact
*Correspondence: wangzhzh@shanghaitech.edu.cn (Z.W.), kaijie.he@innoventbio.com (K.H.)
https://doi.org/10.1016/j.xcrm.2022.100660

SUMMARY

Glucocorticoid-induced tumor necrosis factor receptor (GITR) is a co-stimulatory receptor and an important target for cancer immunotherapy. We herein present a potent FcγR-independent GITR agonist IBI37G5 that can effectively activate effector T cells and synergize with anti-programmed death 1 (PD1) antibody to eradicate established tumors. IBI37G5 depends on both antibody bivalency and GITR homo-dimerization for efficient receptor cross-linking. Functional analyses reveal bell-shaped dose responses due to the unique 2:2 antibody-receptor stoichiometry required for GITR activation. Antibody self-competition is observed after concentration exceeded that of 100% receptor occupancy (RO), which leads to antibody monovalent binding and loss of activity. Retrospective pharmacokinetics/pharmacodynamics analysis demonstrates that the maximal efficacy is achieved at medium doses with drug exposure near saturating GITR occupancy during the dosing cycle. Finally, we propose an alternative dose-finding strategy that does not rely on the traditional maximal tolerated dose (MTD)-based paradigm but instead on utilizing the RO-function relations as biomarker to guide the clinical translation of GITR and similar co-stimulatory agonists.

INTRODUCTION

Although substantial clinical success has been achieved by cancer immunotherapy in recent years, the relatively low overall response rate and inevitable drug resistance in most treated patients are still major challenges in this field.[1] Amplifying the T cell receptor (TCR) downstream signal through activating the co-stimulatory receptors holds great promise to further enhance the efficacy of immunotherapy.[2] Glucocorticoid-induced tumor necrosis factor receptor (GITR) is an important immune co-stimulatory receptor belonging to the tumor necrosis factor receptor superfamily (TNFRSF). It is constitutively expressed on regulatory T (Treg) cells and has low expression on naïve T cells or T memory cells. However, when T cells are activated, GITR expression will be significantly upregulated.[3] Through binding to GITR ligand (GITRL) expressed on the surface of activated antigen-presenting cells (APCs), GITR can activate downstream nuclear factor κB (NF-κB) signals via tumor necrosis factor (TNF) receptor-associated factors (TRAFs), release pro-inflammatory cytokines, and promote T cell proliferations.[4]

In the tumor microenvironment (TME), after tumor specific T cells recognize their cognate tumor antigens through TCR, GITRL functions as a co-stimulatory factor to enhance the effector function and clonal expansion of GITR$^+$ T cells.[5] Exogenous provision of GITRL or GITR agonist antibodies can mimic the role of GITRL in the TME and cross-link GITR receptors to increase the function of CD8$^+$ T cells, thereby enhancing anti-tumor immunity.[6–8] In addition, GITR signals stimulated by GITR agonists can also alleviate the immunosuppressive function of Treg cells by either down-regulating Foxp3 expression or de-differentiation of Treg cells into CD4 effector T cells.[9–11] By Fc-mediated antibody-depedent cellular cytotoxicity (ADCC) functions, GITR antibodies can also selectively deplete GITR high-expressing Treg cells in the TME, thereby skewing the balance in favor of tumor-killing T cells.[12] A number of pre-clinical studies have also proved that GITR agonists combined with other immunotherapies can rescue dysfunctional CD8$^+$ T to promote rapid tumor killing and stimulate the proliferation of precursor effector memory T cells for long-lasting responses in mice.[6,13,14]

Based on these studies, many companies have developed GITR agonists with different mechanisms of action (MOAs),

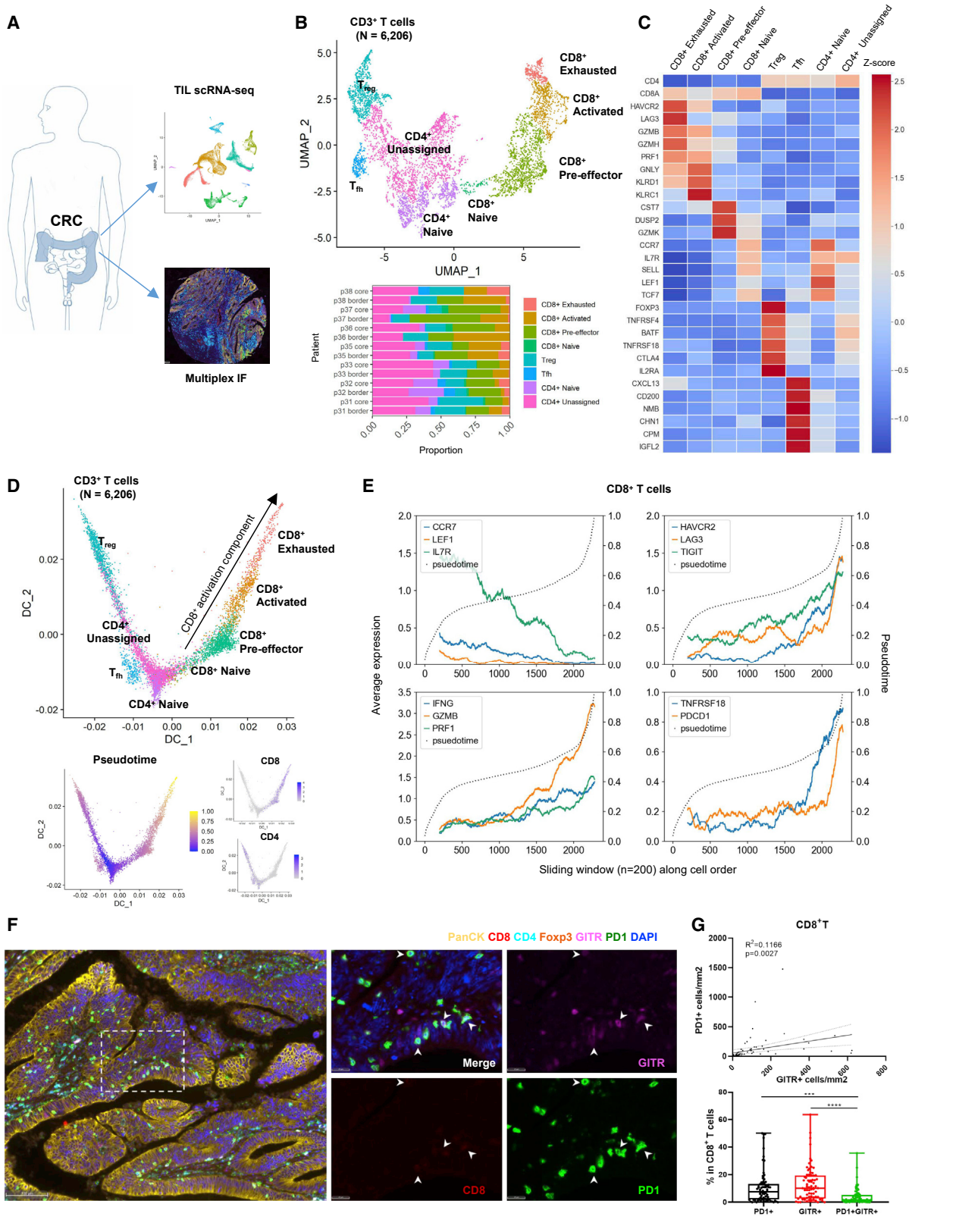

(legend on next page)

and some of them have entered clinical trials.[15] Despite great anti-tumor potential and excellent safety profiles shown in preclinical studies, the clinical efficacy of GITR agonists is usually quite limited in cancer patients. Some pharmacodynamic responses have been observed in early-phase clinical studies; however, objective tumor responses are rarely seen in patients treated with monotherapy.[16–18] Other clinical studies combining GITR agonist and anti-programmed death 1 (PD1) antibodies failed to show synergistic activity, except for one small cohort of immune checkpoint inhibitor (ICI)-naïve (but none in ICI-pretreated) melanoma patients.[19–21] These clinical disappointments have unveiled significant knowledge gaps when extrapolating data from animal models to human patients.[22] Conceivably, the successful clinical translation of GITR agonists may require better understandings of GITR biology in the context of human tumors and demand in-depth mechanistic studies to uncover the key determinants for optimal GITR activation *in vivo* using human-relevant models.[23]

To study these issues, we have characterized an anti-GITR agonist antibody IBI37G5 and investigated its immune-stimulation mechanisms and the pharmacokinetics (PK)/pharmacodynamics (PD) relationships in mouse and monkey models. We have also determined the proper antibody-receptor stoichiometry required for IBI37G5-induced GITR activation and defined the therapeutic window for optimal anti-tumor efficacy based on simulated receptor occupancy-function relations *in vivo*. These findings provide insights into the paradigm of using receptor occupancy (RO)-activity relation for dose selection and facilitate the translation of therapeutics targeting GITR and other co-stimulatory receptors.

RESULTS

Dynamic regulations of GITR and PD1 expression on tumor-infiltrating lymphocytes (TILs) from human CRC

Previous studies have shown that GITR expression is low on human naïve and memory T cells but can be significantly upregulated upon TCR activation, a phenomenon analogous to PD1 expression on T cells.[24,25] This leads us to speculate that GITR and PD1 may share a similar regulation pattern following T cell activation. Indeed, we observed that activation of human peripheral blood mononuclear cells (PBMCs) *in vitro* induced upregulation of both markers (Figures S1A and S1B). To examine the intricate regulation of GITR and PD1 expressions in the TME, we analyzed the publicly available single-cell RNA sequencing (scRNA-seq) data from 14 tumor samples collected from 7 treatment-naïve, stage I to IV colorectal cancer (CRC) patients (Figure S1C)[26] and clustered T cells into 8 distinctive subtypes (Figures 1A–1C). $CD8^+$ T cell clusters show a clear T cell activation trajectory (naïve → pre-effector → activated → exhausted) (Figure 1D). As expected, naïve markers (*CCR7*, *IL7R*, and *LEF1*) decreased along the cell order, while exhaustion markers (*HAVCR2*, *LAG3*, and *TIGIT*) showed the opposite trend (Figure 1E). Effector markers (*GZMB*, *IFNG*, and *PRF1*) increased in parallel with exhaustion markers and reached their peaks near the end of the trajectory, consistent with previous reports that terminally exhausted cells are the primarily cytotoxic $CD8^+$ T cells in the TME.[27,28] In addition, both GITR (TNFRSF18) and PD1 expression increased along the $CD8^+$ T cell activation trajectory, consistent with our *in vitro* finding (Figure 1E). Parallel upregulation of GITR and PD1 was also observed in $CD4^+Foxp3^-$ T cells (Figure S1E). By contrast, GITR and TIGIT expressions in Treg cells continued to rise from already high basal levels while other exhaustion and effector markers remained mostly unchanged (Figure S1E), consistent with the previously reported roles of GITR and TIGIT in Treg cells.[15,29]

To evaluate the co-expression patterns of GITR and PD1 on TILs *in situ*, we performed multiplex fluorescence staining of 75 CRC samples on the tumor microarray chip. $CD8^+$ T cells and $CD4^+Foxp3^-$ T cells account for an average of 53.6% and 42.4% of all T cells, respectively. With an average of only 4%, Treg numbers were inversely correlated with the rate of $CD8^+$ T cell infiltrations (Figure S1F). These results are in line with our scRNA-seq analysis and the previously reported tumor immunohistochemistry data (Figure 1B).[30] $GITR^+$ or $PD1^+$ $CD8^+$ T cells were distributed both in the tumor parenchyma and tumor-associated stroma and were correlated with each other on their respective infiltration levels. Moreover, a substantial proportion of these infiltrated lymphocytes showed $PD1^+GITR^+$ double positivity (Figures 1F and 1G). Similar trends were also observed in $CD4^+Foxp3^-$ T and Treg cells in these tumor samples (Figures S1G–S1I).

Collectively, we found that the regulation of GITR and PD1 expression was highly orchestrated during the activation/exhaustion processes of T cells in CRC. We also noted that

Figure 1. Dynamic regulations of GITR and PD1 expression on TILs from human CRC

(A) Experimental design.

(B–G) Transcriptomic (B–E) and histological analyses (F–G) on tumor-infiltrating lymphocytes (TILs) from human CRC samples.

(B) Uniform manifold approximation and projection (UMAP) representation of $CD3^+$ TIL clusters from 7 CRC patients (top). Fraction of cells in each $CD3^+$ TIL clusters per sample (bottom). p, patient; core, neoplasm core; border, neoplasm border.

(C) Heatmap of differentially expressed genes in $CD3^+$ clusters from (B).

(D) Diffusion map of $CD3^+$ clusters using the first two diffusion components (top). Clusters are colored according to identities in (B). Pseudotime (bottom left) and feature plots for CD8 and CD4 (bottom right) are depicted on the same scale.

(E) Sliding windows (N = 200) of average expression of genes of interest in $CD8^+$ T cells are quantified along the pseudotime cell order.

(F) A representative image showing the localization of $PD1^+GITR^+CD8^+$ T cells (arrow heads) in CRC tissues using multiplex immunohistochemistry (left, scale bar: 100 μm). The inset illustrates higher resolution images (right, scale bar: 25 μm). PanCK (orange) is tumor cell marker, and white depicts merged green (PD1) and purple (GITR).

(G) Quantitation of $PD1^+$, $GITR^+$, and $GITR^+PD1^+$ expression in tumor-infiltrated $CD8^+$ T cells. Each dot represents one tumor sample. Regression analysis showing $PD1^+$ and $GITR^+CD8^+$ T cells numbers per mm^2 (top). p value was calculated automatically by GraphPad software in linear regression module. Box and whiskers plot represents the frequency of expression of PD1 and GITR in $CD8^+$ TILs (bottom). p values were calculated using one-way ANOVA, ***$p < 0.001$, ****$p < 0.0001$.

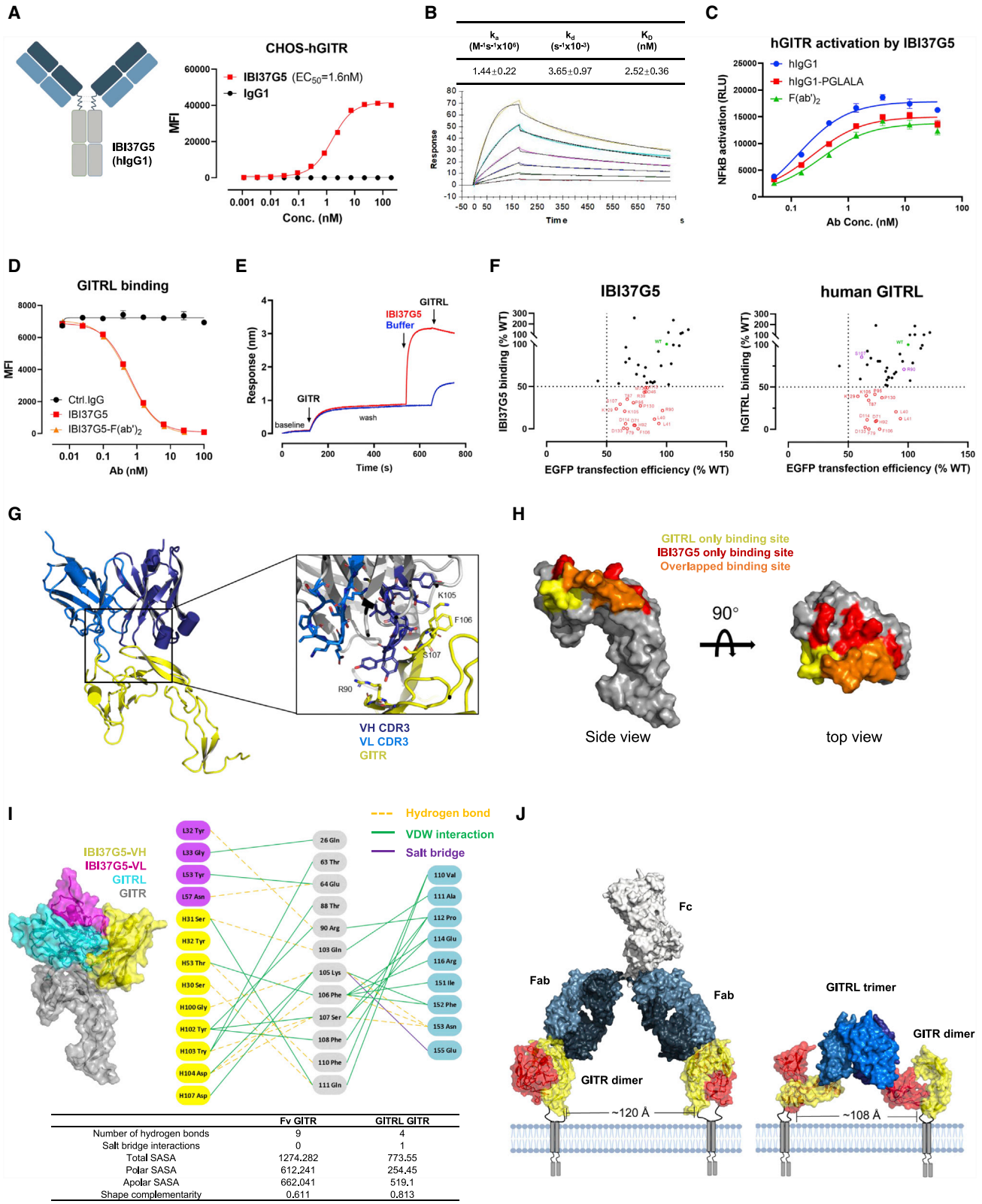

	Fv GITR	GITRL GITR
Number of hydrogen bonds	9	4
Salt bridge interactions	0	1
Total SASA	1274.282	773.55
Polar SASA	612.241	254.45
Apolar SASA	662.041	519.1
Shape complementarity	0.611	0.813

(legend on next page)

GITR may complement PD1 in identifying tumor-specific $CD8^+$ T cells in both mouse and human tumors (Figure S2). These findings underscore the critical function of the co-stimulatory GITR signal, in concert with the inhibitory signals of immune checkpoints, to modulate TCR activation and cytotoxic activities of T cells. Indeed, TCGA data analysis predicts better prognosis in cancer patients with high *TNFSF18* (GITRL) expression in the TME (Figure S1J),[31] further supporting the notion that activating the GITR-GITRL axis is beneficial for anti-tumor immunity.[13,32]

Characterization of IBI37G5, a ligand-mimetic anti-GITR agonist antibody

We previously disclosed an anti-GITR agonist antibody IBI37G5 derived from mouse hybridoma technology.[33] IBI37G5 is a humanized immunoglobulin G1 (IgG1) with high affinity to human GITR (hGITR) (K_D = 2.5 nM) (Figures 2A and 2B) and GITRs from non-human primates (NHPs) (Figures S3A–S3C), but it does not cross-react with species like canines and rodents (Figure S3D). To understand the mechanisms of antibody-mediated GITR agonism, we compared the full-length hIgG1 with the Fc-silent (hIgG1-PGLALA) or -absent ($F(ab')_2$) versions of IBI37G5 in an hGITR-Jurkat reporter assay and found that all of them showed robust agonistic activities (Figure 2C), indicating an Fc-independent function *in vitro*. In the ligand competing experiment, we showed that IBI37G5 (regardless of hIgG1 or $F(ab')_2$) abrogated GITRL binding to hGITR-expression cells at half-maximal effective concentration [EC_{50}] <1 nM (Figure 2D) due to its much higher affinity than GITRL (K_D > 5 μM as reported).[34] Moreover, the epitope-binning assay confirmed competitive binding of IBI37G5 with GITRL (Figure 2E). To determine the epitope of IBI37G5, we performed an alanine-scanning experiment by introducing a mutation to each residue on all possible surface regions of GITR's extracellular domain (ECD) and evaluated how they affect the bindings to antibody. Mutations on nineteen residues lead to reduced binding to IBI37G5 by more than 50%, and all the residues, except R90 and S107, are also required for GITRL binding (Figures 2F and S3E).

To investigate how subtle differences in epitopes between IBI37G5 and GITRL influence the binding affinity and agonistic activity, we computationally modeled the complex structure of variable fragments (Fv) of IBI37G5 and GITR's ECD based on the recently solved GITR crystal structures[34] and our alanine-scanning result (Figures 2G, 2H, and S3F). Our model of the Fv-GITR binding interface highlighted four key amino acids (R90, K105, F106, S107) on GITR that form extensive interactions with residues in CDR3s of both variable heavy (VH) and variable light (VL) regions (Figure 2G). Superimposition of IBI37G5-Fv on the structure of GITRL-GITR complex (PDB: 7KHD) reveals a large overlapping binding area within the conformational epitopes located on the surfaces of CRD2 domain (Figure 2H). The binding interface with total SASA of ~1,274 $Å^2$ comprises an extensive network of hydrophobic interactions, van der Waals (VDW) interactions, and hydrogen bonds that may contribute to the marked difference (~1,000-fold) in affinities, despite a substantially shared binding epitope, between antibody and GITRL (Figure 2I). By computer modeling, we predicted that the bivalent IBI37G5 was able to engage two GITR receptors simultaneously (one GITR by each Fab arm) on the cell membrane based on the statistical analyses of IgG1 antibody conformations.[35] The most probable distance between the C termini of IBI37G5-bound GITR is about 120 Å (range from 90 to 200 Å) (Figure 2J), which is close to the distance of 108 Å observed in the trimeric GITR-GITRL structure, to allow sufficient spacing of GITR intracellular domains for TRAF trimer engagement.

Collectively, these data show that IBI37G5 is a high-affinity ligand-blocking GITR agonist antibody that mimics the mode of action of GITRL to facilitate efficient GITR activation independent of FcγRs.

IBI37G5 combined with PD1 blockade synergistically activates T cells *in vitro* and *in vivo*

To investigate the function of IBI37G5 on T cell activation, we first conducted an *in vitro* human T cell co-stimulation assay. In 2/4 healthy donors, single-agent IBI37G5 induced modest but significant ($p < 0.05$) activation of T cells as measured by interferon gamma (IFN-γ) release (Figure 3A). When combined with anti-PD1 antibody sintilimab (Tyvvt),[36] IBI37G5 significantly enhanced the activity of sintilimab in 3/4 donors. To examine the immune-modulating activities of human-specific antibodies *in vivo*, we used the immunocompetent hPD1/hGITR double knockin mice to test whether IBI37G5 alone or in combinations could promote anti-tumor immunity in syngeneic tumor models. We found that

Figure 2. Characterization of IBI37G5, a ligand-mimetic anti-GITR agonist antibody

(A) Binding of IBI37G5 to CHOS-hGITR cells using fluorescence-activated cell sorting (FACS) analysis.

(B) Kinetic analysis of IBI37G5 binding to hGITR using surface plasmon resonance.

(C) Agonistic activities of different IBI37G5 formats in Jurkat-hGITR NF-κB reporter assay. Graph shows representative results of at least 3 replicate experiments.

(D and E) IBI37G5 competes GITRL binding to GITR in FACS and bio-layer interferometry (BLI) analysis. (D) Competitive binding of IBI37G5 with hGITRL-mFc on Jurkat-hGITR cells. Mean ± SD is presented.

(E) Sandwich ligand-blocking assay showing hGITR/hGITRL interaction blocked by IBI37G5. Representative sensorgrams from duplicate measurements are shown.

(F) Alanine scanning on GITR shows residues required for IBI37B5 or GITRL binding (red) and residues only required for IBI37G5 binding (purple).

(G) Modeled structure of hGITR and Fv (IBI37G5) complex shown in cartoon. hGITR, VH, and VL are colored in yellow, marine, and blue, respectively. Interface residues included in the epitope and CDR3 regions are shown as sticks.

(H) hGITRL, Fv, and overlapped binding regions on hGITR.

(I) Superimposed structures of hGITR/Fv (IBI37G5) and hGITR/hGITRL complexes (left). Schematic diagram elucidated the significant interactions between hGITR (gray) and IBI37G5-VL (magenta) and IBI37G5-VH (yellow) and hGITRL (cyan). Hydrogen bonds, salt bridges, and van der Waals interactions are indicated in orange dashed lines, purple lines, and green lines, respectively (right). The table listed the information of interactions (bottom).

(J) Comparison of modeled receptor-antibody (left) and receptor-ligand (right) complexes shown in surface representation. hGITR/IBI37G5 was modeled based on the most probable conformation of hIgG1. One GITR receptor dimer was masked from hGITR/hGITRL complex to show receptor-ligand interaction. The distance was measured between the C termini of modeled hGITR.

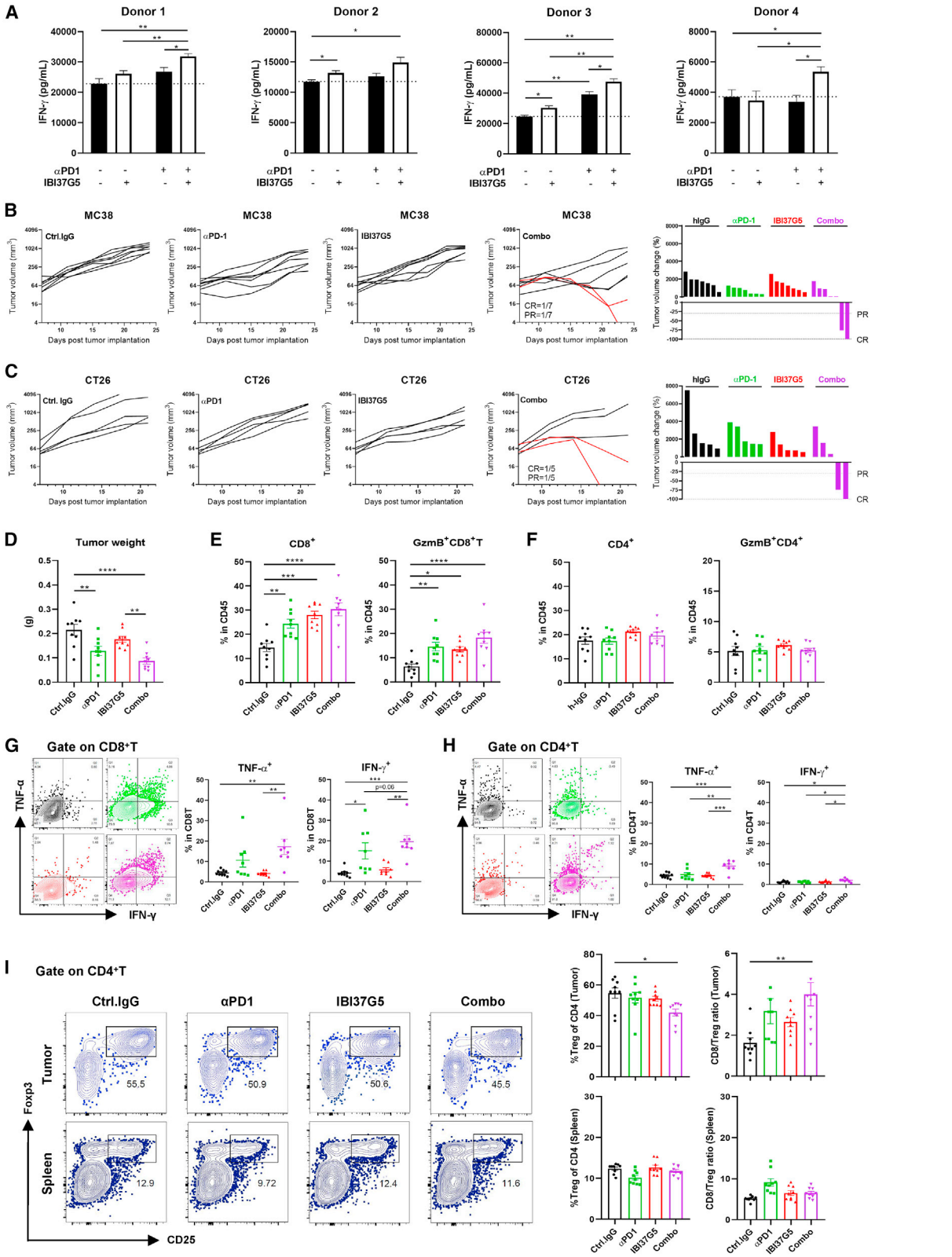

(legend on next page)

in both MC38 and CT26 tumors, the efficacy of either antibody alone was relatively weak, showing only modest tumor-growth delay. However, in the combination-treatment group, we observed significant tumor regressions, suggesting a synergistic effect (Figures 3B and 3C). To better understand the underlying mechanism, we analyzed the phenotypes and functionalities of TILs in MC38 tumors 1 week post drug treatment. The tumor weight changes were consistent with the above efficacy studies during the short treatment cycle, showing best activities in the combination group (Figure 3D). In addition, the proportions of total tumor-infiltrating $CD8^+$ T cells and cytotoxic $GzmB^+CD8^+$ T cells after combination therapy were both highest among all treatment groups (Figure 3E). However, no such changes were observed in the tumor-infiltrated $CD4^+$ T cells (Figure 3F). To examine how different therapy affects the polyfunctionalities of tumor-specific T cells, we isolated the TILs from MC38 tumors and analyzed their intracellular production of effector molecules after stimulation with the autologous tumor cells *ex vivo*. Increased productions of IFN-γ and TNF-α by $CD8^+$ and $CD4^+$ TILs were detected, to various extents, in all treatment groups compared with IgG control, with TILs after combination therapy showing highest induction levels (Figures 3G and 3H). Despite the comparable expressions at baseline, both the proportions and absolute numbers of $CD8^+$ TILs positive for single (GzmB) or double effector parameters (IFN-γ and TNF-α) were much higher than that of $CD4^+$ TILs (Figures 3E–3H and S4). Together, these data suggest that the tumor-specific $CD8^+$ TILs, as well as a smaller $CD4^+$ subset, exhibited the potential for activation, infiltration, and cytotoxicity after combination therapy of anti-GITR and anti-PD1 antibodies, which led to the *in vivo* anti-tumor efficacy.

Previous studies have reported that GITR activation could down-regulate Foxp3 expression and inhibit the immunosuppressive activity of Treg cells[37] and that GITR antibodies could also deplete $GITR^{high}$ Treg cells in the TME through Fc-mediated ADCC functions.[12] As IBI37G5 has a strong GITR activation effect and adopts an ADCC-competent hIgG1-Fc,[38] we speculate that IBI37G5 may exert anti-tumor efficacy (at least partially) by modulating Treg functions. But, unexpectedly, IBI37G5 treatment did not affect either Foxp3 levels or Treg percentages in $CD4^+$ T cells from mouse tumors or spleens (Figure 3I). A small, but significant, decrease of Treg percentage was observed only in the combination group, possibly due to some indirect effects that negatively affected the Treg availability in the pro-inflammatory TME after immune stimulation.[39,40] These data are in sharp contrast to the reported mechanisms of mouse GITR antibody DTA-1, which can effectively deplete Treg cells through ADCC functions alongside its effector T cell activation activity.[15] Due to species differences, the affinities of hIgG1 to mouse FcγRs are several orders of magnitude lower than that of humans (Figure S5A). Moreover, the markedly elevated expression of inhibitory receptor (mFcγRIIb) on tumor-associated macrophages and dendritic cells (DCs), along with the less dramatic increase of activatory receptor (mFcγRIII) on tumor-infiltrating natural killer (NK) cells, may further decrease the activatory-to-inhibitory (A/I) ratio of hIgG1 (Figures S5B and S5C), rendering its ADCC activity less potent in the immune-suppressive TME.[41,42] To investigate whether the lack of Treg depletion by IBI37G5 is due to the compromised ADCC activity of hIgG1 in mouse tumors, we replaced the hIgG1-Fc portion of IBI37G5 with the mouse Fc equivalent to create a chimeric IBI37G5-mIgG2a with higher mFcγR affinities and A/I ratios (Figure S5A) and then examined how the Fc portion of different IgGs would affect Treg depletion efficiency and anti-tumor activity. Consistent with previous data, IBI37G5 monotherapy had only marginal anti-tumor activity regardless of its Fc subtypes (Figure S5D), and the higher affinities of mIgG2a to mFcγRs did not translate into notable Treg depletions despite high levels of GITR on Treg cells (Figures S5E and S5F), suggesting a different MOA of IBI37G5 from the previously reported Treg-depletion GITR antibodies. Interestingly, a significant drop of GITR, but not Foxp3, levels on $CD4^+$ T cells were observed in mice treated with either Fc subtype of IBI37G5 (Figure S5F), in line with previous clinical findings of dramatic GITR downregulation, yet there was no Treg depletion after GITR-antibody treatments.[17] The lack of Treg-depletion activity of IBI37G5 could be partially explained by the rapid antibody-mediated receptor endocytosis (Figures S5G and S5H), which may lead to reduced ADCC efficiency in animals,[43] although other factors affecting ADCC functions such as binding epitope/kinetics and *in situ* antibody exposures still remain to be determined.[44]

Collectively, we show that IBI37G5 could work in conjunction with PD1 antibody to directly activate effector T cells, especially cytotoxic $CD8^+$ T cells, but less likely function through depleting Treg cells, to exert anti-tumor effects.

GITR homodimerization and antibody bivalency are both required for the agonistic activity of IBI37G5

Recently, Wang et al. reported that both mouse- and hGITR have pre-ligand assembly domain (PLAD)-like sequences at the membrane-proximal CRD3 domain to enable the formation of

Figure 3. IBI37G5 combined with PD1 blockade synergistically activates T cells *in vitro* and *in vivo*

(A) Human T cell activations after indicated treatments were determined by measuring released IFN-γ in the supernatant. Biological replicates from 4 different donors were shown.

(B and C) Individual tumor growth curves post treatments in MC38- (B) or CT26- (C) inoculated mice. Mice were randomized at day 7 when tumor volume reached around 60–80 mm^3 before being treating with αPD1 (0.5 mg/kg) or IBI37G5 (1 mg/kg) twice weekly. The waterfall plots show tumor volume changes by the end of study. Tumor complete regression was defined as CR, and tumor volume reduced >30% from baseline was defined as PR. N = 5–7 mice in each group.

(D–F) Tumor weight (D) and percentage of tumor-infiltrating $CD8^+$ T cells (E) or $CD4^+$ T cells (F).

(D–I) Mice bearing MC38 tumors were treated with indicated antibodies and sacrificed 1 week post treatment.

(G and H) Representative FACS plots and bar graphs showing intracellular staining of TNF-α and IFN-γ in $CD8^+$ TILs (G) and $CD4^+$ TILs (H) after *ex vivo* stimulation with MC38 cells.

(I) Representative FACS plots of Treg cell populations in tumors and spleens of mice after treatments. Bar graphs showing Treg cell percentage in $CD4^+$ T cells and ratio of $CD8^+$ T/Treg in tumors and spleens. Each dot represents one mouse (N = 9 mice/group). Mean ± SEM is presented, and p values were calculated using one-way ANOVA, *p < 0.05, **p < 0.01, ***p < 0.001, ****p < 0.0001.

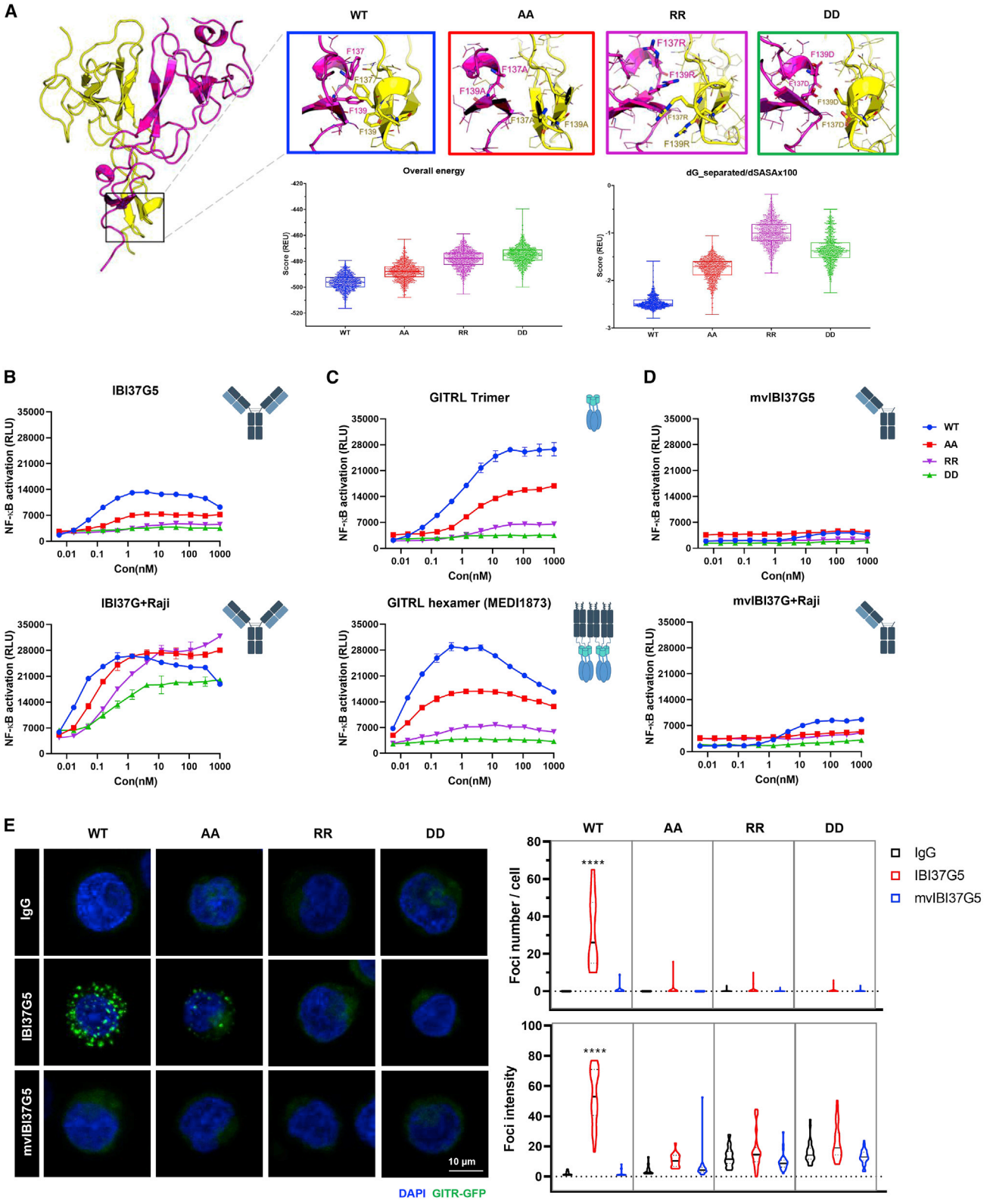

(legend on next page)

homodimer structures through non-covalent interactions,[34] which resembles the N-terminal PLAD-mediated receptor clustering in other TNFR family members.[45] Homodimer structure is necessary for ligand-dependent formation of high-order GITR clustering and downstream signal amplification. Given the mechanistic similarities between IBI37G5 and GITRL, we speculate that IBI37G5 also requires GITR-receptor dimerization to exert its agonistic activity. To test this hypothesis, we introduced amino-acid mutations on two critical phenylalanine residues (F137 and F139) simultaneously into alanines (AA), arginines (RR), or aspartic acids (DD) to reduce or abolish the receptor-receptor hydrophobic interface and examined how these changes might affect the activity of GITR agonists. *In silico*, we modeled three GITR mutants and analyzed their interface binding energy. These GITR dimer mutants had higher overall energy and dG_separated/dSASA (the binding energy per unit interface surface area) and were more difficult to form stable homodimers than wild-type GITR (Figure 4A). In Jurkat NF-κB reporter cells expressing GITR receptors (wild type [WT] or mutants) (Figure S6A), the capability of IBI37G5 to activate downstream signaling was positively correlated with the feasibility of GITR variants to form homodimers: GITR(WT)>GITR(AA)>GITR(RR)∼GITR(DD) (Figure 4B, top). A similar trend was also observed with GITRL trimer and high-valency GITR agonist MEDI1873 (Figure 4C). Although FcγR-mediated cross-linking was not required for function, the agonistic activity of IBI37G5 in reporter cells expressing all GITR variants was dramatically amplified by FcγR-expressing Raji cells (Figure 4B, bottom). Notably, signal transductions of GITR interface mutants were largely rescued to the activity levels approaching WT-GITR by Raji co-cultures, suggesting that FcγR-mediated secondary cross-linking can overcome the defects of mutant GITRs in insufficient oligomerization after IBI37G5 stimulation. In comparison, the structure of the membrane-proximal domain of another TNFRSF member 4-1BB is highly homologous to GITR but lacks the hydrophobic interface needed for receptor homodimerization (Figure S6C). After replacing this hydrophobic region on CRD3 of GITR with a corresponding 4-1BB fragment, we found a near-complete loss of IBI37G5 activity, which was rescuable by Raji cross-linking (Figures S6D and S6E), reinforcing the notion that, in contrast to 4-1BB, the ability of receptor homodimer formation was indispensable for GITR activation.

Previous studies have shown that, unlike antagonist antibodies, TNFRSF agonist antibodies usually require bivalency or even higher valency to exert activity.[46] Considering the similarities shared by TNFRSF members, we postulate that IBI37G5 also requires antibody bivalency for activity. To this end, we designed a monovalent form of IBI37G5 (mvIBI37G5) and tested its activity on different GITR variants. As expected, the GITR agonistic activity was almost completely abolished in the mvIBI37G5 form. Even with Raji co-culturing, the activity of mvIBI37G5 could only be slightly restored in WT-GITR-expressing reporter cells but not in other homodimer-interface mutants (Figure 4D). Moreover, we used confocal microscopy to directly visualize and quantitate the capability of IBI37G5 to induce receptor oligomerization. Jurkat cells expressing WT-GITR-GFP fusion proteins showed strong induction of receptor clustering as measured by increased GFP foci numbers and fluorescence intensities after IBI37G5 treatment (Figure 4E). In contrast, neither GITR interface mutant-expressing nor mvIBI37G5-treated cells exhibited measurable foci formation, except scattered foci of smaller sizes and weaker intensities were detected in IBI37G5-treated GITR(AA)-Jurkat cells, in line with its weak residual activity in the reporter assays.

Collectively, we show that IBI37G5 promotes GITR oligomerization and activation in a way that highly resembles GITRL, which is dependent on both receptor homodimerization and antibody bivalency for high-order receptor clustering and signal amplifications in T cells.

IBI37G5 induces a bell-shaped dose response *in vitro*

In the Jurkat reporter assay, we observed that when the concentration of IBI37G5 (or GITRL trimer) exceeded that of peak activity, the NF-κB signal began to decrease rather than reaching a plateau, presenting a bell-shaped response that is reminiscent of some previously reported agonist antibodies.[47,48] We speculated that this phenomenon was due to the intrinsic properties of bivalent IBI37G5 rather than being Fc related (Figure S7A). As the NF-κB reporter system is an artificial system that cannot truly reflect the immediate changes of GITR downstream signal in human T cells, we isolated $CD4^+$ T cells from PBMCs and then co-stimulated these *Staphylococcus enterotoxin B* (SEB)-primed T cells with IBI37G5 before detection of NF-κB p65 phosphorylation. With the rise of IBI37G5 concentrations, the phosphorylation levels of NF-κB in $GITR^+CD4^+$ T cells gradually elevated and later peaked at 37 nM. But after the peak, a continued trend of decreasing activities was observed despite the increase of drug concentrations up to 1,000 nM. In contrast, the phosphorylation of NF-κB in $GITR^-CD4^+$ T cells, as an internal control, remained unchanged during the treatment course, suggesting a target-specific effect of IBI37G5-induced bell-shaped GITR activation *in vitro* (Figure 5A). Similar results of phosphorylation on two different sites (S536 and S529) of NF-κB p65 in Jurkat-GITR cells were also observed (Figure S7B).

Figure 4. GITR homodimerization and antibody bivalency are both required for the agonistic activity of IBI37G5

(A) The cartoon models of WT dimeric hGITR and mutants when mutating two critical interface residues F137 and F139 into alanines (AA), arginines (RR), or aspartic acids (DD). The mutated residues are shown as sticks. Overall stability and interface energy density of WT dimeric hGITR and mutants were calculated by ROSETTA relax application.

(B–D) Activities of GITR agonists: IBI37G5 (B), GITRL trimer or GITRL hexamer MEDI1873 (C), or monovalent (mv) IBI37G5 (D) measured in Jurkat NF-κB reporter cells expressing WT or mutant GITRs. Mean ± SD is presented.

(E) Confocal images showing GITR receptor clustering on Jurkat cells expressing WT or mutant GITRs upon indicated treatments at 10 nM. Scale bar: 10 μm. Quantification of GFP foci number and intensity (cell number = 20–50). Mean florescence intensity of foci or diffused cytoplasmic GFP signal was measured. Median (50%) and quartiles (25%, 75%) were shown in violin plots. Experiments were repeated at least twice. p values were calculated using one-way ANOVA, ****$p < 0.0001$.

Conceivably, at the optimal dose, an antibody-receptor stoichiometric balance is established when two Fab arms of the same antibody simultaneously occupy two different GITR receptors in a 2:2 stoichiometry to facilitate higher order receptor cross-linking. By contrast, at higher concentrations, the existing balance is disrupted when antibodies self-compete for receptor binding. In this case, only one Fab of each antibody is able to engage GITR, while the other arm remains unoccupied and ineffective and somewhat mirrors the binding mode of mvIBI37G5, thereby resulting in insufficient receptor activation. To test this hypothesis, we designed an experiment to detect the dynamic changes of RO and antibody self-competition by measuring the abundance of antibodies bound to GITR$^+$ T cells and the availability of free Fabs of GITR-bound antibodies on the cell surface, respectively. We found that the binding signal of IBI37G5 on activated CD4$^+$ T cells reached saturation at concentrations exceeding 12 nM (Figure 5B, bottom), which was in line with the RO assay that showed near-zero GITR availability on human T cells after pre-incubation with IBI37G5 at 22 nM or higher, indicating 100% RO beyond this concentration point (Figure S7C). By using AF647-labeled GITR-ECD protein to measure the free Fabs of GITR-bound IBI37G5, we detected only baseline signals on T cells pre-treated with IBI37G5 at concentrations below the receptor-saturating point, suggesting that no detectable Fabs were exposed due to the avid, bivalent binding of IBI37G5 to GITR. However, at higher concentrations of saturating GITR occupancy, a marked increase of the GITR-ECD-AF647 signal was detected, indicating the exposure of free Fabs due to self-competition and monovalent binding of IBI37G5 to GITR receptors (Figure 5B, top). Similar results were also obtained in the experiments analyzing different T cell subsets of PBMCs (Figure S7D).

To examine whether different levels of antibody-RO would affect GITR oligomerization on the cell membrane, we used confocal imaging to visualize the receptor cluster formation on Jurkat-GITR-GFP cells. The strongest receptor cross-linking (shown as GFP foci) was observed at the concentration of optimal RO (~10 nM), while at higher concentrations, both the GFP foci numbers and fluorescent signals decreased significantly, consistent with above mentioned results in reporter assays (Figures 5C and 5D). To further investigate the RO-function relationships in primary human T cells, we assessed the immunomodulatory activities of IBI37G5 in human CD4$^+$ T cells. In all four donors, the T cell activation markers (CD25 and CD69) and the release of effector cytokines (interleukin-2 [IL-2] and IFN-γ) were all upregulated after IBI37G5 treatment and peaked within the concentration range of 11–33 nM but declined at 100 nM, echoing the previous findings (Figure 5E). Furthermore, in the multiplex human PBMC cytokine release assay, a similar trend of dose response was also observed (Figure S7E).

Besides IBI37G5, we also tested other clinical-stage TNFRSF agonist antibodies, TRX518 (anti-GITR), pogalizumab (anti-OX40), and urelumab (anti-4-1BB), in their respective Jurkat reporter assays. All of these antibodies exhibited bell-shaped dose responses (Figure S7F), suggesting the universality of this phenomenon among TNFRSF agonists.

The bell-shaped anti-tumor response of IBI37G5 is associated with the level of GITR receptor saturation *in vivo*

To study whether the *in vitro*-defined RO-function relationship also prevails in animals, we tested the anti-tumor efficacy of IBI37G5 as single agent or in combination with anti-PD1 antibody in different tumor models. In the MC38 tumors, IBI37G5 alone only showed weak activities, while the combination group exhibited marked tumor-growth delays as well as tumor regressions in animals (Figures 6A and S8A). Notably, IBI37G5 at 1 mg/kg combined with anti-PD1 antibody showed best efficacy, including 25% (3/12) tumor free in treated mice. By contrast, at higher doses, the incremental benefit of drug combination was diminished at 3 mg/kg or near abrogated at 10 mg/kg compared with anti-PD1 monotherapy, suggesting the loss of IBI37G5 activities at high exposure levels *in vivo* (Figures 6A–6C). Next, we validated these findings in another anti-PD1-resistant B16F10 tumor model. Despite no tumor regressions, the most dramatic tumor-growth inhibition was found in 1 mg/kg IBI37G5-treated mice (Figures 6D, 6E, and S8B).

To establish the *in vivo* PK/PD relationship, we performed a PK study of IBI37G5 in hGITR knockin mice. Although there was a higher clearance rate at low dose (0.3 mg/kg) due to the antigen-sink effect, IBI37G5 exhibited a trend of linear exposure at doses above 1 mg/kg (Figures 6F and S8C). Interestingly, we found that the exposure level of IBI37G5 at 1 mg/kg covered the range of optimal activities (10–100 nM, blue shade) in the majority of the weekly dosing cycles. By contrast, due to the fast clearance at 0.3 mg/kg, the systemic exposure rapidly fell outside the optimal range after the first 24 h. Nevertheless, the systemic exposures of IBI37G5 at 3 and 10 mg/kg exceeded that of optimal range, leading to complete saturation of GITR RO throughout the dosing cycle (Figure S8D). We speculate that, analogous to our *in vitro* findings, constant (over-)saturation of GITR by high IBI37G5 concentrations *in vivo* could also lead to antibody self-competition and insufficient engagement with GITR and thereby affect the anti-tumor efficacy. By analyzing the RO-efficacy relation, we saw that the near-saturated RO of GITR at 1 mg/kg conferred best anti-tumor activities in both models, recapitulating the bell-shaped dose responses *in vivo* (Figure 6G).

Together, these results indicate that the optimal target saturation during the dosing cycle is a key determinant factor for allowing IBI37G5 to fully engage and activate GITR in a proper antibody-receptor stoichiometry, which is more beneficial for achieving maximal anti-tumor efficacy than insufficient or over saturation of GITR receptors.

PK/PD and toxicology studies of IBI37G5 in NHPs

To better predict human responses, we carried out the good laboratory practice (GLP) PK/PD and toxicology studies in NHPs. IBI37G5 showed a typical monoclonal antibody PK profile with long terminal half-life and dose-dependent exposures to support at least biweekly dosing in humans (Figures S9A and S9B). After repeated IBI37G5 administrations, the percentages of different T cell subsets in the peripheral blood did not change compared with the control group (Figure S9C). Consistent with the findings in mice, no meaningful reductions of Foxp3 expressions or total Treg cell numbers were observed after drug treatment, further

CellPress
OPEN ACCESS

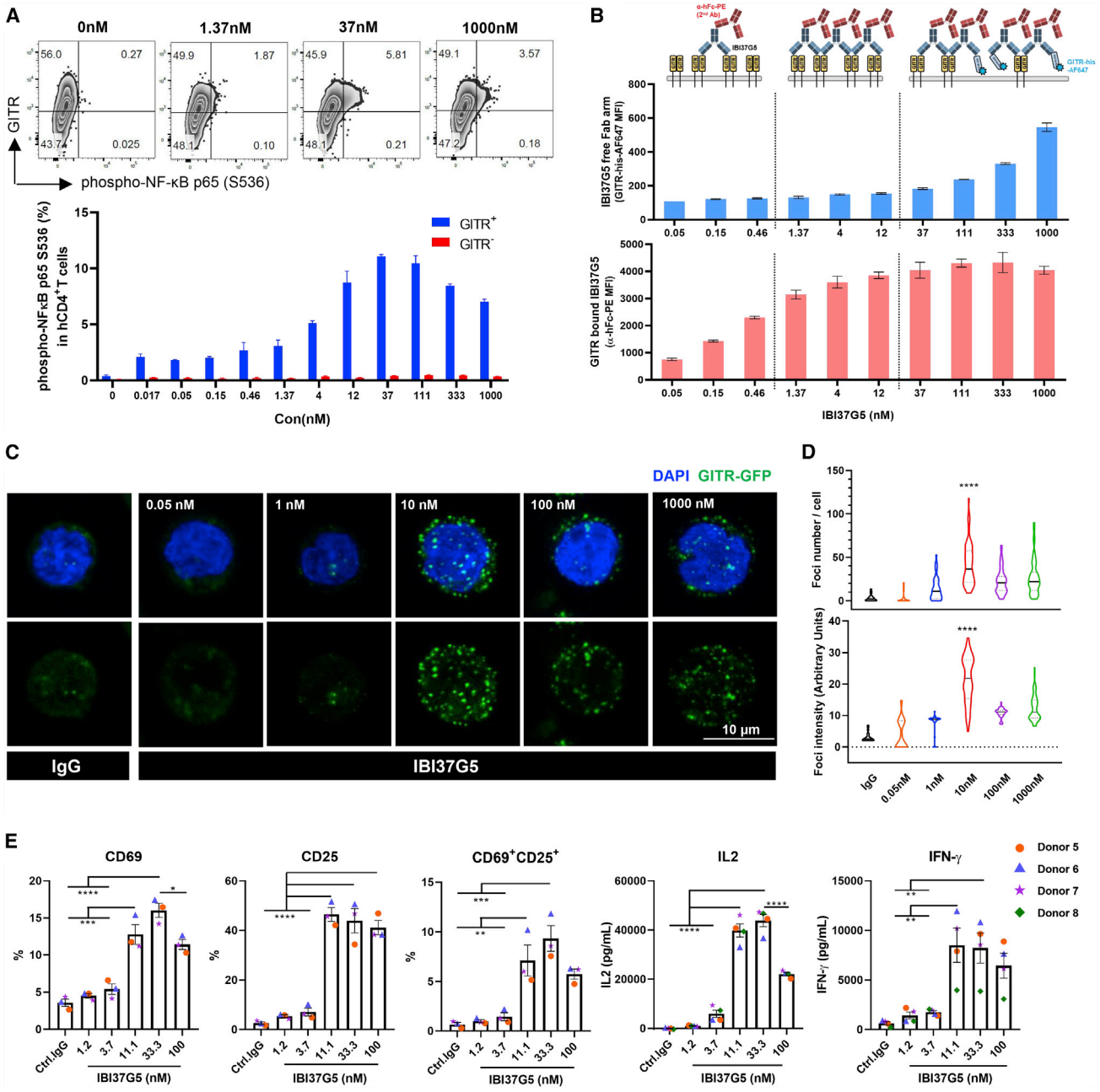

Figure 5. IBI37G5 induces a bell-shaped dose response *in vitro*

(A) Bell-shaped response of IBI37G5 in human CD4+ T cells. SEB-primed human CD4+ T cells were incubated with IBI37G5 for 5 min, and NF-κB p65 phosphorylation was detected by flow cytometry.

(B) Detection of freely exposed Fabs of IBI37G5 at different levels of target saturation.

(C) GITR receptor clustering upon IgG or IB37G5 treatment at different concentrations. Scale bar: 10 μm.

(D) Quantification of foci number and intensity by GFP florescence (cell number = 23–66). Mean florescence intensity of foci (cells with foci formation) or diffused cytoplasmic GFP signal (cells without foci) was measured. Median (50%) and quartiles (25%, 75%) were shown in violin plots. Experiments were performed in duplicate.

(E) Bell-shaped response induced by IBI37G5 in human CD4+ T cell activation and functional analyses. Experiments were performed in triplicate using T cells from 4 healthy donors. Mean ± SEM is presented, and p values were calculated using one-way ANOVA, *p < 0.05, **p < 0.01, ***p < 0.001, ****p < 0.0001.

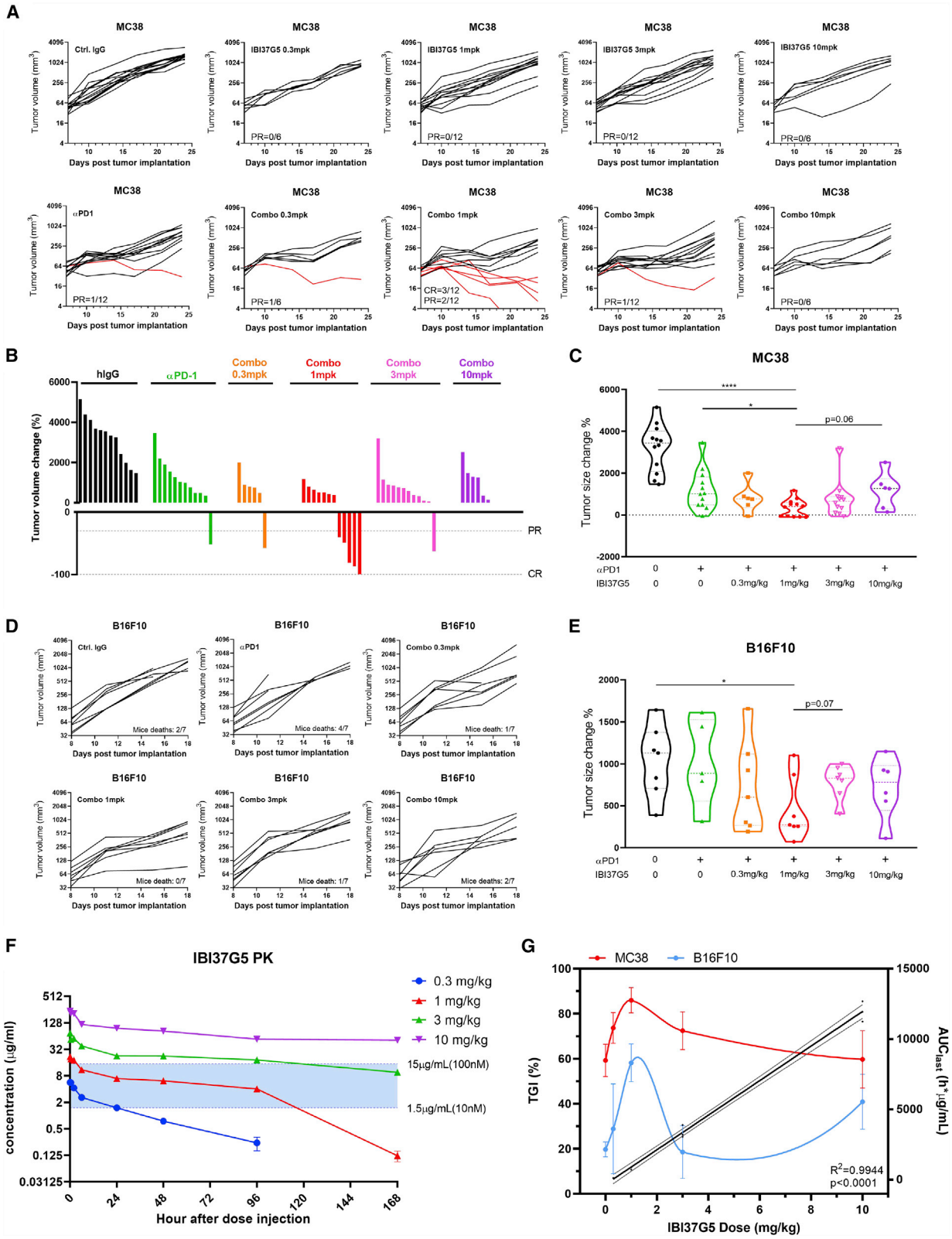

(legend on next page)

substantiating the Treg-independent mechanisms of IBI37G5. More importantly, IBI37G5 was well tolerated after repeated doses in monkeys, and the maximal tolerated dose (MTD) was not defined in this study. No drug-related serious clinical symptoms were recorded, and the hematology and blood biochemistry parameters were all within the normal range despite minor fluctuations (data not shown). Most cytokines were maintained at their pre-treated baselines, except the evident increase of IL-6 (although one to two orders of magnitude lower than that in cytokine release syndrome [CRS][49]) in monkey plasma (Figure S9D). Few significant toxic effects were seen in the major organs at postmortem examinations except for some abnormalities in thymus and adrenal gland in the highest-dose group (Figure S9E).

DISCUSSION

Co-stimulatory antibodies that enhance anti-tumor immunity have great potential in cancer therapy. But until now, successful translation of these therapies into patients still remains a big challenge, due to either insufficient efficacy or severe immune-related toxicities.[50] In-depth research on the MOAs of immune agonists is of great significance to better guide their clinical development. In this study, we characterized an anti-GITR agonist antibody IBI37G5 and studied its molecular mechanisms using primary human cells and human gene knockin animals. Unlike many TNFRSF agonist antibodies that non-competitively stabilize the pre-formed receptor-ligand complex and/or require Fc-mediated secondary cross-linking for efficient signal transduction,[46,51] IBI37G5 is unique in that the high-affinity ligand-competitive antibody is able to directly induce robust GITR clustering and downstream signaling through bivalent Fab-receptor engagement, independent of ligand co-binding or Fc-related functions. In many cases, antibodies that fully block the receptor-ligand interactions exhibit antagonistic, rather than agonistic, activities,[52,53] so how IBI37G5 induces strong GITR agonism is an intriguing question. Recent studies have shown that by simply switching the IgG isotypes (hIgG1 → hIgG2), the CD40 antagonists can be converted into strong agonists,[54] possibly due to the hIgG2-mediated higher binding avidity and strong self-association tendency upon antigen binding.[55] Although such self-association has been previously described for other human IgG isotypes,[56,57] it is less likely that IBI37G5 exerts its agonistic activity through similar mechanism due to the much weaker self-association capability of hIgG1. In addition, the assembly of IgG1 oligomers is dependent on Fc-Fc interactions,[58] but the Fc-absent $F(ab')_2$ of IBI37G5 is fully functional, therefore excluding the effects of IgG self-assembly on agonist activity. Rather, these results suggest that the intrinsic binding properties of IBI37G5, such as kinetics, epitope, and stoichiometry, could be the key determinants for the unique MOAs that distinguish it from other TNFRSF agonists.

Through epitope mapping and *in silico* antibody-receptor docking, we show that IBI37G5 recognizes GITR at an epitope largely overlapping with GITRL. It is able to maintain proper spacing between receptors on the cell membrane to form complexes that resemble the basic signaling units reported in other TNFRSFs.[59] The high affinity of IBI37G5 enables avid, bivalent engagement of GITR homodimers, which may further increase the chance of free IBI37G5 to successfully link and stabilize two individual antibody-receptor complexes and drive higher-order receptor clustering (Figure 7A). In contrast to other well-studied TNFRSF agonists, this model suggests a different mechanism that the natural ligands are dispensable and that the pre-arranged receptor-ligand complexes are not required for IBI37G5-induced receptor activation. Particularly, IBI37G5 can mimic the function of GITRL to pre-assemble and then cross-link the basic signal units. The correct stoichiometry between IBI37G5 and GITR is essential for efficient receptor oligomerization and signal amplification (Figures 7A–7C). However, despite the similarities between IBI37G5 and GITRL, their differences in valency may greatly impact the stoichiometry of receptor-ligand complexes and the manner of higher-order signaling network formation on the cell membrane. Based on the crystal structures of GITR, Wang et al. proposed that the hGITR-GITRL complex can form a hexagonal "honeycomb-like" grid consisting of six GITRL trimers and six GITR trimers.[34] In contrast, the bivalent IBI37G5 is geometrically improbable to gather GITR receptors into a similar branched hexameric structure. Contrary to the trimeric form of hGITRL, mouse GITRLs favor the biologically active dimer conformation. The C-terminal three-residue deleted mGITRLs can form activity-enhanced trimers,[60] indicating that both human and mouse GITRLs can utilize various oligmeric forms (including dimer, trimer, and even superclusters) to fine-tune the receptor activations.[61] Likewise, bivalent IBI37G5 serves as a hyperactive surrogate of hGITRL dimer (Figure S6B) and has 2:2 stoichiometry that resembles the murine GITR-GITRL interactions. As to whether the antibody-receptor complexes form a linear chained structure or higher-dimensional

Figure 6. The bell-shaped antitumor response of IBI37G5 is associated with the level of GITR receptor saturation *in vivo*

(A–C) Antitumor activity of IBI37G5 as monotherapy or in combination with anti-PD1 antibody in MC38 tumor model. Mice (N = 6 mice/group) were treated with antibodies at indicated doses twice weekly for 5 times. Pooled data from two independent experiments were shown.

(A) Individual tumor growth curves in mice from different treatment groups. Red curves highlight tumor regressions (CR or PR).

(B) Waterfall plots showing tumor size changes at the end of study.

(C) Individual, median (50%), and quartiles (25%, 75%) of tumor size change were shown in violin plots.

(D and E) Anti-tumor activity of IBI37G5 in combination with anti-PD1 antibody in B16F10 tumor model. N = 7 mice/group, twice weekly dosing for 4 times.

(F) Pharmacokinetics of IBI37G5 in mice. IBI37G5 at indicated doses were administered intravenously in hGITR knockin mice (N = 9 mice/group), and blood samples from indicated time points were collected and analyzed using sandwich ELISA. Dotted lines and blue areas in between depict the antibody concentration range matching the best *in vitro* activities.

(G) PK/PD simulation of IBI37G5 in tumor models. Red (MC38) and blue (B16F10) curves show bell-shaped correlation between tumor-growth-inhibition percentage (TGI%) at different doses of IBI37G5 (left y axis). Regression analysis of IBI37G5 exposure levels (area under curve [AUC]) and dosages shows strong positive correlation (right y axis). Mean ± SEM is presented, and p values were calculated using one-way ANOVA, *p < 0.05, **p < 0.01, ***p < 0.001, ****p < 0.0001.

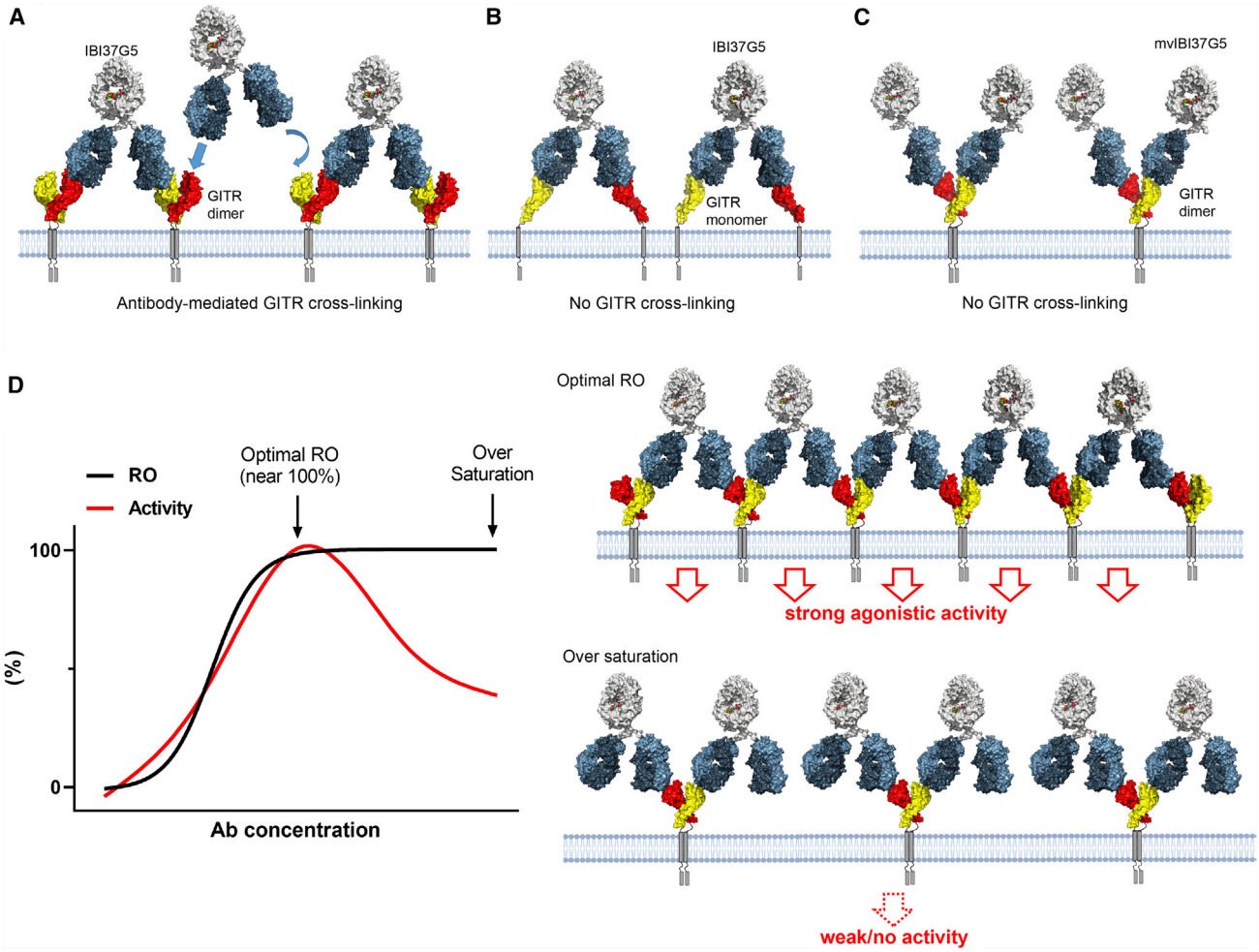

Figure 7. Proposed working models

(A) IBI37G5 binds two GITR dimers simultaneously to form the basic signaling unit-like complex on the cell membrane in a 2:2 stoichiometry, and free IBI37G5 antibody can engage and link two pre-arranged complexes to form higher-order cross-linking for signal transduction.

(B) If GITR were not able to form homodimer (due to disrupted dimeric interface on CRD3), IBI37G5 can only engage two GITR monomers but is unable to induce GITR cross-linking.

(C) mvIBI37G5 can only bind one GITR dimer and fails to form GITR cross-linking.

(D) Hypothetical dose-dependent RO-activity relationship of IBI37G5 on GITR agonism (left). At optimal RO, IBI37G5 links GITR dimers to form a linear chained network to transduce robust downstream signaling (top right). At oversaturated RO, IBI37G5 binds to GITR in a monovalent pose and only induces weak GITR agonism due to failed receptor cross-linking (bottom right).

oligomerization networks remain to be determined in future studies.

The instances of bell-shaped dose responses have been reported in many drug classes.[62–64] For immunostimulatory antibodies, many studies have investigated the mechanisms underlying this phenomenon through *in vitro* experiments, and various explanations were proposed.[65] However, whether these theories can be verified in animal models, or even in clinical studies, remain to be explored. In this work, we have defined the stoichiometry of the antibody-receptor complex and established an RO-function relationship that determines the optimal GITR activations. These findings were validated in different murine syngeneic tumor models. To our best knowledge, it is the first attempt to investigate the bell-shaped anti-tumor responses based on the dynamic changes of RO-activity relations (Figure 7D). Potentially, our study proposes a strategy for developing practical biomarkers to predict patient response and guide the clinical dose determination of immune co-stimulators that share similar MOAs. In the GLP toxicology studies, IBI37G5 showed linear PK and excellent safety profiles at exposure levels much higher than the efficacious dose, enabling its clinical translation in cancer patients. The human PK profiles can be projected from the monkey data alongside the clinical results of other GITR agonists using the interspecies allometric-scaling methods.[66,67] It is reasonable to expect that IBI37G5 is able to achieve high exposures with acceptable tolerability in patients. If the predicted exposure significantly exceeds that of optimal efficacious dose, we should consider the possibility of bell-shaped dose

responses and the impact on the outcomes of clinical trials. In designing the dose-escalation trial, it would be beneficial to integrate the RO-activity relation as a component of PD biomarkers and correlate this PD effect with early clinical signs of efficacy to identify the recommended phase 2 dose (RP2D) rather than simply relying on the MTD-based paradigm of dose selection in the traditional oncology drug developments.[68]

In conclusion, despite hurdles in clinical translation, the ample pre-clinical evidence and signs of clinical response have demonstrated the promise of GITR agonists in cancer treatment. Given the unique properties of immune agonist antibodies, the dynamic RO-response-based approaches for PK/PD prediction and efficacious dose finding may be essential for the successful development of this drug class. In this respect, strategies described herein will be explored in future clinical studies to help unlock the full therapeutic potential of IBI37G5, and possibly other costimulatory agonists, in cancer patients.

Limitations of the study

First, the correlation between RO and anti-tumor efficacy was established based on the *in vitro* activity experiments and the retrospective PK/PD analysis in mice. Its prediction accuracy requires further validations in larger-scale animal experiments or even in clinical settings. Second, in contrast to using mouse surrogate antibodies or humanized mice with partially reconstituted immune system, immunocompetent hGITR/hPD1 double knockin mice were utilized in our study to better investigate the functions of human specific antibodies. However, the conclusions derived from these mouse models still need to be interpreted cautiously given the notable differences between human and mouse GITRs in both the expression profiles and functionalities.[24,69] Finally, this study combined scRNA-seq data mining and multiplex immunofluorescence to analyze the spatiotemporal dynamics of GITR and PD1 in TILs of CRC. It would be interesting to explore whether tumors with increased TILs co-expressing GITR and PD1 benefit more from combination therapy. In addition, whether the dynamic changes of co-expression patterns can be extrapolated to other tumor types, and whether the expression levels of GITR-GITRL axis in the TME can be used as biomarkers to predict therapeutic efficacy or drug resistance are issues worthy of further exploration.

STAR★METHODS

Detailed methods are provided in the online version of this paper and include the following:

- KEY RESOURCES TABLE
- RESOURCE AVAILABILITY
  - Lead contact
  - Materials availability
  - Data and code availability
- EXPERIMENTAL MODEL AND SUBJECT DETAILS
  - Cell lines
  - Animals
  - Human PBMCs
- METHOD DETAILS
  - *In vitro* assays
  - *In silico* analysis
  - *In vivo* studies
- QUANTIFICATION AND STATISTICAL ANALYSIS

SUPPLEMENTAL INFORMATION

Supplemental information can be found online at https://doi.org/10.1016/j.xcrm.2022.100660.

ACKNOWLEDGMENTS

We thank Dr. Yong-Jun Liu for helpful discussions, Dr. Renzhen Lai for consultation on statistical analyses, and the Innovent GITR project team for hybridoma screening and antibody selection. This work was supported by the Innovent Guoqing Academy discovery research fund to K.H. and a ShanghaiTech University Startup grant to W.X.

AUTHOR CONTRIBUTIONS

Conceptualization, K.H.; *in vitro* experiments, H.L., X.L., J.G., Z.K., and L.H.; pharmacology & toxicology, W.W., L.C., Y.Y., J.W., J.L., M.W., D.W., and B.C.; protein sciences, F.F., Z. Wu, S.Z., and Z.S.; structural analysis, G.S., W.X., and Z. Wang; bioinformatics, T.C.; writing – original draft, K.H.; writing – review & editing, all authors; supervision, K.H. and Z. Wang.

DECLARATION OF INTERESTS

H.L., W.W., T.C., L.C., X.L., J.G., F.F., Y.Y., Z. Wu, S.Z., J.W., J.L., Z.K., M.W., Z.S., L.H., D.W., B.C., and K.H. are current employees and own stocks of Innovent Biologics (Suzhou) Co., Ltd. F.F. is co-inventor of GITR antibodies used in this study (patent no. WO2019201301A1).

Received: December 8, 2021
Revised: March 26, 2022
Accepted: May 20, 2022
Published: June 21, 2022

REFERENCES

1. Restifo, N.P., Smyth, M.J., and Snyder, A. (2016). Acquired resistance to immunotherapy and future challenges. Nat. Rev. Cancer *16*, 121–126. https://doi.org/10.1038/nrc.2016.2.
2. Chen, L., and Flies, D.B. (2013). Molecular mechanisms of T cell co-stimulation and co-inhibition. Nat. Rev. Immunol. *13*, 227–242. https://doi.org/10.1038/nri3405.
3. Shevach, E.M., and Stephens, G.L. (2006). The GITR-GITRL interaction: co-stimulation or contrasuppression of regulatory activity? Nat. Rev. Immunol. *6*, 613–618. https://doi.org/10.1038/nri1867.
4. Buzzatti, G., Dellepiane, C., and Del Mastro, L. (2019). New emerging targets in cancer immunotherapy: the role of GITR. ESMO Open *4*, e000738. https://doi.org/10.1136/esmoopen-2020-000738.
5. van Beek, A.A., Zhou, G., Doukas, M., Boor, P.P.C., Noordam, L., Mancham, S., Campos Carrascosa, L., van der Heide-Mulder, M., Polak, W.G., Ijzermans, J.N.M., et al. (2019). GITR ligation enhances functionality of tumor-infiltrating T cells in hepatocellular carcinoma. Int. J. Cancer *145*, 1111–1124. https://doi.org/10.1002/ijc.32181.
6. Leyland, R., Watkins, A., Mulgrew, K.A., Holoweckyj, N., Bamber, L., Tigue, N.J., Offer, E., Andrews, J., Yan, L., Mullins, S., et al. (2017). A novel murine GITR ligand fusion protein induces antitumor activity as a monotherapy that is further enhanced in combination with an OX40 agonist. Clin. Cancer Res. *23*, 3416–3427. https://doi.org/10.1158/1078-0432.CCR-16-2000.
7. Durham, N.M., Holoweckyj, N., MacGill, R.S., McGlinchey, K., Leow, C.C., and Robbins, S.H. (2017). GITR ligand fusion protein agonist enhances the tumor antigen-specific CD8 T-cell response and leads to long-lasting

memory. J. Immunother. Cancer *5*, 47. https://doi.org/10.1186/s40425-017-0247-0.

8. Bulliard, Y., Jolicoeur, R., Windman, M., Rue, S.M., Ettenberg, S., Knee, D.A., Wilson, N.S., Dranoff, G., and Brogdon, J.L. (2013). Activating Fc gamma receptors contribute to the antitumor activities of immunoregulatory receptor-targeting antibodies. J. Exp. Med. *210*, 1685–1693. https://doi.org/10.1084/jem.20130573.

9. Stephens, G.L., McHugh, R.S., Whitters, M.J., Young, D.A., Luxenberg, D., Carreno, B.M., Collins, M., and Shevach, E.M. (2004). Engagement of glucocorticoid-induced TNFR family-related receptor on effector T cells by its ligand mediates resistance to suppression by CD4+CD25+ T cells. J. Immunol. *173*, 5008–5020. https://doi.org/10.4049/jimmunol.173.8.5008.

10. Xiao, X., Shi, X., Fan, Y., Zhang, X., Wu, M., Lan, P., Minze, L., Fu, Y.X., Ghobrial, R.M., Liu, W., and Li, X.C. (2015). GITR subverts Foxp3(+) Tregs to boost Th9 immunity through regulation of histone acetylation. Nat. Commun. *6*, 8266. https://doi.org/10.1038/ncomms9266.

11. Amoozgar, Z., Kloepper, J., Ren, J., Tay, R.E., Kazer, S.W., Kiner, E., Krishnan, S., Posada, J.M., Ghosh, M., Mamessier, E., et al. (2021). Targeting Treg cells with GITR activation alleviates resistance to immunotherapy in murine glioblastomas. Nat. Commun. *12*, 2582. https://doi.org/10.1038/s41467-021-22885-8.

12. Mahne, A.E., Mauze, S., Joyce-Shaikh, B., Xia, J., Bowman, E.P., Beebe, A.M., Cua, D.J., and Jain, R. (2017). Dual roles for regulatory T-cell depletion and costimulatory signaling in agonistic GITR targeting for tumor immunotherapy. Cancer Res. *77*, 1108–1118. https://doi.org/10.1158/0008-5472.CAN-16-0797.

13. Wang, B., Zhang, W., Jankovic, V., Golubov, J., Poon, P., Oswald, E.M., Gurer, C., Wei, J., Ramos, I., Wu, Q., et al. (2018). Combination cancer immunotherapy targeting PD-1 and GITR can rescue CD8(+) T cell dysfunction and maintain memory phenotype. Sci. Immunol. *3*, eaat7061. https://doi.org/10.1126/sciimmunol.aat7061.

14. Ko, K., Yamazaki, S., Nakamura, K., Nishioka, T., Hirota, K., Yamaguchi, T., Shimizu, J., Nomura, T., Chiba, T., and Sakaguchi, S. (2005). Treatment of advanced tumors with agonistic anti-GITR mAb and its effects on tumor-infiltrating Foxp3+CD25+CD4+ regulatory T cells. J. Exp. Med. *202*, 885–891. https://doi.org/10.1084/jem.20050940.

15. Knee, D.A., Hewes, B., and Brogdon, J.L. (2016). Rationale for anti-GITR cancer immunotherapy. Eur. J. Cancer *67*, 1–10. https://doi.org/10.1016/j.ejca.2016.06.028.

16. Balmanoukian, A.S., Infante, J.R., Aljumaily, R., Naing, A., Chintakuntlawar, A.V., Rizvi, N.A., Ross, H.J., Gordon, M., Mallinder, P.R., Elgeioushi, N., et al. (2020). Safety and clinical activity of MEDI1873, a novel GITR agonist, in advanced solid tumors. Clin. Cancer Res. *26*, 6196–6203. https://doi.org/10.1158/1078-0432.CCR-20-0452.

17. Tran, B., Carvajal, R.D., Marabelle, A., Patel, S.P., LoRusso, P.M., Rasmussen, E., Juan, G., Upreti, V.V., Beers, C., Ngarmchamnanrith, G., and Schoffski, P. (2018). Dose escalation results from a first-in-human, phase 1 study of glucocorticoid-induced TNF receptor-related protein agonist AMG 228 in patients with advanced solid tumors. J. Immunother. Cancer *6*, 93. https://doi.org/10.1186/s40425-018-0407-x.

18. Zappasodi, R., Sirard, C., Li, Y., Budhu, S., Abu-Akeel, M., Liu, C., Yang, X., Zhong, H., Newman, W., Qi, J., et al. (2019). Rational design of anti-GITR-based combination immunotherapy. Nat. Med. *25*, 759–766. https://doi.org/10.1038/s41591-019-0420-8.

19. Heinhuis, K.M., Carlino, M., Joerger, M., Di Nicola, M., Meniawy, T., Rottey, S., Moreno, V., Gazzah, A., Delord, J.P., Paz-Ares, L., et al. (2020). Safety, tolerability, and potential clinical activity of a glucocorticoid-induced TNF receptor-related protein agonist alone or in combination with nivolumab for patients with advanced solid tumors: a phase 1/2a dose-escalation and cohort-expansion clinical trial. JAMA Oncol. *6*, 100–107. https://doi.org/10.1001/jamaoncol.2019.3848.

20. Papadopoulos, K.P., Autio, K., Golan, T., Dobrenkov, K., Chartash, E., Chen, Q., Wnek, R., and Long, G.V. (2021). Phase I study of MK-4166, an anti-human glucocorticoid-induced TNF receptor antibody, alone or with pembrolizumab in advanced solid tumors. Clin. Cancer Res. *27*, 1904–1911. https://doi.org/10.1158/1078-0432.CCR-20-2886.

21. Geva, R., Voskoboynik, M., Dobrenkov, K., Mayawala, K., Gwo, J., Wnek, R., Chartash, E., and Long, G.V. (2020). First-in-human phase 1 study of MK-1248, an anti-glucocorticoid-induced tumor necrosis factor receptor agonist monoclonal antibody, as monotherapy or with pembrolizumab in patients with advanced solid tumors. Cancer *126*, 4926–4935. https://doi.org/10.1002/cncr.33133.

22. Zloza, A., Karolina Palucka, A., Coussens, L.M., Gotwals, P.J., Headley, M.B., Jaffee, E.M., Lund, A.W., Sharpe, A.H., Sznol, M., Wainwright, D.A., et al. (2017). Workshop on challenges, insights, and future directions for mouse and humanized models in cancer immunology and immunotherapy: a report from the associated programs of the 2016 annual meeting for the Society for Immunotherapy of cancer. J. Immunother. Cancer *5*, 77. https://doi.org/10.1186/s40425-017-0278-6.

23. Romero, D. (2019). SABR improves outcomes. Nat. Rev. Clin. Oncol. *16*, 402. https://doi.org/10.1038/s41571-019-0217-1.

24. Sukumar, S., Wilson, D.C., Yu, Y., Wong, J., Naravula, S., Ermakov, G., Riener, R., Bhagwat, B., Necheva, A.S., Grein, J., et al. (2017). Characterization of MK-4166, a clinical agonistic antibody that targets human GITR and inhibits the generation and suppressive effects of T regulatory cells. Cancer Res. *77*, 4378–4388. https://doi.org/10.1158/0008-5472.CAN-16-1439.

25. Simon, S., and Labarriere, N. (2017). PD-1 expression on tumor-specific T cells: friend or foe for immunotherapy? Oncoimmunology *7*, e1364828. https://doi.org/10.1080/2162402X.2017.1364828.

26. Qian, J., Olbrecht, S., Boeckx, B., Vos, H., Laoui, D., Etlioglu, E., Wauters, E., Pomella, V., Verbandt, S., Busschaert, P., et al. (2020). A pan-cancer blueprint of the heterogeneous tumor microenvironment revealed by single-cell profiling. Cell Res *30*, 745–762. https://doi.org/10.1038/s41422-020-0355-0.

27. Horton, B.L., Williams, J.B., Cabanov, A., Spranger, S., and Gajewski, T.F. (2018). Intratumoral $CD8^+$ T-cell apoptosis is a major component of T-cell dysfunction and impedes antitumor immunity. Cancer Immunol. Res. *6*, 14–24. https://doi.org/10.1158/2326-6066.Cir-17-0249.

28. Miller, B.C., Sen, D.R., Al Abosy, R., Bi, K., Virkud, Y.V., LaFleur, M.W., Yates, K.B., Lako, A., Felt, K., Naik, G.S., et al. (2019). Subsets of exhausted CD8(+) T cells differentially mediate tumor control and respond to checkpoint blockade. Nat. Immunol. *20*, 326–336. https://doi.org/10.1038/s41590-019-0312-6.

29. Wing, J.B., Tay, C., and Sakaguchi, S. (2019). Control of regulatory T cells by Co-signal molecules. Adv. Exp. Med. Biol. *1189*, 179–210. https://doi.org/10.1007/978-981-32-9717-3_7.

30. Vence, L., Bucktrout, S.L., Fernandez Curbelo, I., Blando, J., Smith, B.M., Mahne, A.E., Lin, J.C., Park, T., Pascua, E., Sai, T., et al. (2019). Characterization and comparison of GITR expression in solid tumors. Clin. Cancer Res. *25*, 6501–6510. https://doi.org/10.1158/1078-0432.CCR-19-0289.

31. Tang, Z., Li, C., Kang, B., Gao, G., Li, C., and Zhang, Z. (2017). GEPIA: a web server for cancer and normal gene expression profiling and interactive analyses. Nucleic Acids Res. *45*, W98–W102. https://doi.org/10.1093/nar/gkx247.

32. Richards, D.M., Marschall, V., Billian-Frey, K., Heinonen, K., Merz, C., Redondo Muller, M., Sefrin, J.P., Schroder, M., Sykora, J., Fricke, H., et al. (2019). HERA-GITRL activates T cells and promotes anti-tumor efficacy independent of $Fc\gamma R$-binding functionality. J. Immunother. Cancer *7*, 191. https://doi.org/10.1186/s40425-019-0671-4.

33. Zhai, T.F., Huang Fenggen., Liu, Weifeng., Junjian. (2018). Anti-gitr Antibody and Use Thereof. WIPO (World Intellectual Property Organization) patent WO2019201301A1, filed April 18, 2019, and published October 24, 2019.

34. Wang, F., Chau, B., West, S.M., Kimberlin, C.R., Cao, F., Schwarz, F., Aguilar, B., Han, M., Morishige, W., Bee, C., et al. (2021). Structures of mouse and human GITR-GITRL complexes reveal unique TNF superfamily interactions. Nat. Commun. *12*, 1378. https://doi.org/10.1038/s41467-021-21563-z.

35. Zhang, X., Zhang, L., Tong, H., Peng, B., Rames, M.J., Zhang, S., and Ren, G. (2015). 3D structural fluctuation of IgG1 antibody revealed by individual particle electron tomography. Scientific Rep. *5*, 9803. https://doi.org/10.1038/srep09803.

36. Hoy, S.M. (2019). Sintilimab: first global approval. Drugs *79*, 341–346. https://doi.org/10.1007/s40265-019-1066-z.

37. Schaer, D.A., Budhu, S., Liu, C., Bryson, C., Malandro, N., Cohen, A., Zhong, H., Yang, X., Houghton, A.N., Merghoub, T., and Wolchok, J.D. (2013). GITR pathway activation abrogates tumor immune suppression through loss of regulatory T cell lineage stability. Cancer Immunol. Res. *1*, 320–331. https://doi.org/10.1158/2326-6066.CIR-13-0086.

38. Shields, R.L., Namenuk, A.K., Hong, K., Meng, Y.G., Rae, J., Briggs, J., Xie, D., Lai, J., Stadlen, A., Li, B., et al. (2001). High resolution mapping of the binding site on human IgG1 for Fc gamma RI, Fc gamma RII, Fc gamma RIII, and FcRn and design of IgG1 variants with improved binding to the Fc gamma R. J. Biol. Chem. *276*, 6591–6604. https://doi.org/10.1074/jbc.M009483200.

39. Overacre-Delgoffe, A.E., Chikina, M., Dadey, R.E., Yano, H., Brunazzi, E.A., Shayan, G., Horne, W., Moskovitz, J.M., Kolls, J.K., Sander, C., et al. (2017). Interferon-gamma drives Treg fragility to promote anti-tumor immunity. Cell *169*, 1130–1141.e11. https://doi.org/10.1016/j.cell.2017.05.005.

40. Sharma, M., Khong, H., Fa'ak, F., Bentebibel, S.E., Janssen, L.M.E., Chesson, B.C., Creasy, C.A., Forget, M.A., Kahn, L.M.S., Pazdrak, B., et al. (2020). Bempegaldesleukin selectively depletes intratumoral Tregs and potentiates T cell-mediated cancer therapy. Nat. Commun. *11*, 661. https://doi.org/10.1038/s41467-020-14471-1.

41. Nimmerjahn, F., and Ravetch, J.V. (2005). Divergent immunoglobulin g subclass activity through selective Fc receptor binding. Science *310*, 1510–1512. https://doi.org/10.1126/science.1118948.

42. Arce Vargas, F., Furness, A.J.S., Solomon, I., Joshi, K., Mekkaoui, L., Lesko, M.H., Miranda Rota, E., Dahan, R., Georgiou, A., Sledzinska, A., et al. (2017). Fc-optimized anti-CD25 depletes tumor-infiltrating regulatory T cells and synergizes with PD-1 blockade to eradicate established tumors. Immunity *46*, 577–586. https://doi.org/10.1016/j.immuni.2017.03.013.

43. Chew, H.Y., De Lima, P.O., Gonzalez Cruz, J.L., Banushi, B., Echejoh, G., Hu, L., Joseph, S.R., Lum, B., Rae, J., O'Donnell, J.S., et al. (2020). Endocytosis inhibition in humans to improve responses to ADCC-mediating antibodies. Cell *180*, 895–914.e27. https://doi.org/10.1016/j.cell.2020.02.019.

44. Tang, Y., Lou, J., Alpaugh, R.K., Robinson, M.K., Marks, J.D., and Weiner, L.M. (2007). Regulation of antibody-dependent cellular cytotoxicity by IgG intrinsic and apparent affinity for target antigen. J. Immunol. *179*, 2815–2823. https://doi.org/10.4049/jimmunol.179.5.2815.

45. Chan, F.K.M., Chun, H.J., Zheng, L., Siegel, R.M., Bui, K.L., and Lenardo, M.J. (2000). A domain in TNF receptors that mediates ligand-independent receptor assembly and signaling. Science *288*, 2351–2354. https://doi.org/10.1126/science.288.5475.2351.

46. Wajant, H. (2015). Principles of antibody-mediated TNF receptor activation. Cell Death Differ *22*, 1727–1741. https://doi.org/10.1038/cdd.2015.109.

47. White, A.L., Chan, H.T., French, R.R., Willoughby, J., Mockridge, C.I., Roghanian, A., Penfold, C.A., Booth, S.G., Dodhy, A., Polak, M.E., et al. (2015). Conformation of the human immunoglobulin G2 hinge imparts superagonistic properties to immunostimulatory anticancer antibodies. Cancer Cell *27*, 138–148. https://doi.org/10.1016/j.ccell.2014.11.001.

48. Stebbings, R., Findlay, L., Edwards, C., Eastwood, D., Bird, C., North, D., Mistry, Y., Dilger, P., Liefooghe, E., Cludts, I., et al. (2007). "Cytokine storm" in the phase I trial of monoclonal antibody TGN1412: better understanding the causes to improve preclinical testing of immunotherapeutics. J. Immunol. *179*, 3325–3331. https://doi.org/10.4049/jimmunol.179.5.3325.

49. Suntharalingam, G., Perry, M.R., Ward, S., Brett, S.J., Castello-Cortes, A., Brunner, M.D., and Panoskaltsis, N. (2006). Cytokine storm in a phase 1 trial of the anti-CD28 monoclonal antibody TGN1412. N. Engl. J. Med. *355*, 1018–1028. https://doi.org/10.1056/NEJMoa063842.

50. Choi, Y., Shi, Y., Haymaker, C.L., Naing, A., Ciliberto, G., and Hajjar, J. (2020). T-cell agonists in cancer immunotherapy. J. Immunother. Cancer *8*, e000966. https://doi.org/10.1136/jitc-2020-000966.

51. Graves, J.D., Kordich, J.J., Huang, T.H., Piasecki, J., Bush, T.L., Sullivan, T., Foltz, I.N., Chang, W., Douangpanya, H., Dang, T., et al. (2014). Apo2L/TRAIL and the death receptor 5 agonist antibody AMG 655 cooperate to promote receptor clustering and antitumor activity. Cancer Cell *26*, 177–189. https://doi.org/10.1016/j.ccr.2014.04.028.

52. Yu, X., Chan, H.T.C., Orr, C.M., Dadas, O., Booth, S.G., Dahal, L.N., Penfold, C.A., O'Brien, L., Mockridge, C.I., French, R.R., et al. (2018). Complex interplay between epitope specificity and isotype dictates the biological activity of anti-human CD40 antibodies. Cancer Cell *33*, 664–675.e4. https://doi.org/10.1016/j.ccell.2018.02.009.

53. Edner, N.M., Carlesso, G., Rush, J.S., and Walker, L.S.K. (2020). Targeting co-stimulatory molecules in autoimmune disease. Nat. Rev. Drug Discov. *19*, 860–883. https://doi.org/10.1038/s41573-020-0081-9.

54. Yu, X., Chan, H.C., Fisher, H., Penfold, C.A., Kim, J., Inzhelevskaya, T., Mockridge, C.I., French, R.R., Duriez, P.J., Douglas, L.R., et al. (2020). Isotype switching converts anti-CD40 antagonism to agonism to elicit potent antitumor activity. Cancer Cell *37*, 850–866.e7. https://doi.org/10.1016/j.ccell.2020.04.013.

55. Yu, X., James, S., Felce, J.H., Kellermayer, B., Johnston, D.A., Chan, H.T.C., Penfold, C.A., Kim, J., Inzhelevskaya, T., Mockridge, C.I., et al. (2021). TNF receptor agonists induce distinct receptor clusters to mediate differential agonistic activity. Commun. Biol. *4*, 772. https://doi.org/10.1038/s42003-021-02309-5.

56. Strasser, J., de Jong, R.N., Beurskens, F.J., Wang, G., Heck, A.J.R., Schuurman, J., Parren, P.W.H.I., Hinterdorfer, P., and Preiner, J. (2019). Unraveling the macromolecular pathways of IgG oligomerization and complement activation on antigenic surfaces. Nano Lett. *19*, 4787–4796. https://doi.org/10.1021/acs.nanolett.9b02220.

57. Rispens, T., Ooievaar-De Heer, P., Vermeulen, E., Schuurman, J., van der Neut Kolfschoten, M., and Aalberse, R.C. (2009). Human IgG4 binds to IgG4 and conformationally altered IgG1 via Fc-Fc interactions. J. Immunol. *182*, 4275–4281. https://doi.org/10.4049/jimmunol.0804338.

58. Strasser, J., de Jong, R.N., Beurskens, F.J., Schuurman, J., Parren, P.W.H.I., Hinterdorfer, P., and Preiner, J. (2020). Weak fragment crystallizable (Fc) domain interactions drive the dynamic assembly of IgG oligomers upon antigen recognition. ACS Nano *14*, 2739–2750. https://doi.org/10.1021/acsnano.9b08347.

59. Vanamee, E.S., and Faustman, D.L. (2018). Structural principles of tumor necrosis factor superfamily signaling. Sci. Signal. *11*, eaao4910. https://doi.org/10.1126/scisignal.aao4910.

60. Zhou, Z., Tone, Y., Song, X., Furuuchi, K., Lear, J.D., Waldmann, H., Tone, M., Greene, M.I., and Murali, R. (2008). Structural basis for ligand-mediated mouse GITR activation. Proc. Natl. Acad. Sci. U S A *105*, 641–645. https://doi.org/10.1073/pnas.0711206105.

61. Zhou, Z., Song, X., Berezov, A., Zhang, G., Li, Y., Zhang, H., Murali, R., Li, B., and Greene, M.I. (2008). Human glucocorticoid-induced TNF receptor ligand regulates its signaling activity through multiple oligomerization states. Proc. Natl. Acad. Sci. U S A *105*, 5465–5470. https://doi.org/10.1073/pnas.0711350105.

62. Fisher, T.S., Kamperschroer, C., Oliphant, T., Love, V.A., Lira, P.D., Doyonnas, R., Bergqvist, S., Baxi, S.M., Rohner, A., Shen, A.C., et al. (2012). Targeting of 4-1BB by monoclonal antibody PF-05082566 enhances T-cell function and promotes anti-tumor activity. Cancer

Immunol. Immunother. *61*, 1721–1733. https://doi.org/10.1007/s00262-012-1237-1.

63. Lühder, F., Huang, Y., Dennehy, K.M., Guntermann, C., Müller, I., Winkler, E., Kerkau, T., Ikemizu, S., Davis, S.J., Hanke, T., and Hünig, T. (2003). Topological requirements and signaling properties of T cell-activating, anti-CD28 antibody superagonists. J. Exp. Med. *197*, 955–966. https://doi.org/10.1084/jem.20021024.
64. Owen, S.C., Doak, A.K., Ganesh, A.N., Nedyalkova, L., McLaughlin, C.K., Shoichet, B.K., and Shoichet, M.S. (2014). Colloidal drug formulations can explain "bell-shaped" concentration–response curves. ACS Chem. Biol. *9*, 777–784. https://doi.org/10.1021/cb4007584.
65. Mayes, P.A., Hance, K.W., and Hoos, A. (2018). The promise and challenges of immune agonist antibody development in cancer. Nat. Rev. Drug Discov. *17*, 509–527. https://doi.org/10.1038/nrd.2018.75.
66. Wang, J., Iyer, S., Fielder, P.J., Davis, J.D., and Deng, R. (2016). Projecting human pharmacokinetics of monoclonal antibodies from nonclinical data: comparative evaluation of prediction approaches in early drug development. Biopharm. Drug Dispos *37*, 51–65. https://doi.org/10.1002/bdd.1952.
67. Nair, A.B., and Jacob, S. (2016). A simple practice guide for dose conversion between animals and human. J. Basic Clin. Pharm. *7*, 27–31. https://doi.org/10.4103/0976-0105.177703.
68. Sachs, J.R., Mayawala, K., Gadamsetty, S., Kang, S.P., and de Alwis, D.P. (2016). Optimal dosing for targeted therapies in oncology: drug development cases leading by example. Clin. Cancer Res. *22*, 1318–1324. https://doi.org/10.1158/1078-0432.Ccr-15-1295.
69. Chattopadhyay, K., Ramagopal, U.A., Brenowitz, M., Nathenson, S.G., and Almo, S.C. (2008). Evolution of GITRL immune function: murine GITRL exhibits unique structural and biochemical properties within the TNF superfamily. Proc. Natl. Acad. Sci. U S A *105*, 635–640. https://doi.org/10.1073/pnas.0710529105.
70. Hao, Y., Hao, S., Andersen-Nissen, E., Mauck, W.M., 3rd, Zheng, S., Butler, A., Lee, M.J., Wilk, A.J., Darby, C., Zager, M., et al. (2021). Integrated analysis of multimodal single-cell data. Cell *184*, 3573–3587.e29. https://doi.org/10.1016/j.cell.2021.04.048.
71. Wolf, F.A., Angerer, P., and Theis, F.J. (2018). SCANPY: large-scale single-cell gene expression data analysis. Genome Biol. *19*, 15. https://doi.org/10.1186/s13059-017-1382-0.
72. Virtanen, P., Gommers, R., Oliphant, T.E., Haberland, M., Reddy, T., Cournapeau, D., Burovski, E., Peterson, P., Weckesser, W., Bright, J., et al. (2020). SciPy 1.0: fundamental algorithms for scientific computing in Python. Nat. Methods *17*, 261–272. https://doi.org/10.1038/s41592-019-0686-2.
73. Lu, D., Liu, L., Ji, X., Gao, Y., Chen, X., Liu, Y., Liu, Y., Zhao, X., Li, Y., Li, Y., et al. (2015). The phosphatase DUSP2 controls the activity of the transcription activator STAT3 and regulates TH17 differentiation. Nat. Immunol. *16*, 1263–1273. https://doi.org/10.1038/ni.3278.
74. Yang, R., Cheng, S., Luo, N., Gao, R., Yu, K., Kang, B., Wang, L., Zhang, Q., Fang, Q., Zhang, L., et al. (2019). Distinct epigenetic features of tumor-reactive CD8+ T cells in colorectal cancer patients revealed by genome-wide DNA methylation analysis. Genome Biol. *21*, 2. https://doi.org/10.1186/s13059-019-1921-y.
75. Song, Y., DiMaio, F., Wang, R.R., Kim, D., Miles, C., Brunette, T., Thompson, J., and Baker, D. (2013). High-resolution comparative modeling with RosettaCM. Structure *21*, 1735–1742. https://doi.org/10.1016/j.str.2013.08.005.
76. Weitzner, B.D., Jeliazkov, J.R., Lyskov, S., Marze, N., Kuroda, D., Frick, R., Adolf-Bryfogle, J., Biswas, N., Dunbrack, R.L., Jr., and Gray, J.J. (2017). Modeling and docking of antibody structures with Rosetta. Nat. Protoc. *12*, 401–416. https://doi.org/10.1038/nprot.2016.180.
77. Kozakov, D., Hall, D.R., Xia, B., Porter, K.A., Padhorny, D., Yueh, C., Beglov, D., and Vajda, S. (2017). The ClusPro web server for protein-protein docking. Nat. Protoc. *12*, 255–278. https://doi.org/10.1038/nprot.2016.169.
78. Sircar, A., and Gray, J.J. (2010). SnugDock: paratope structural optimization during antibody-antigen docking compensates for errors in antibody homology models. PLoS Comput. Biol. *6*, e1000644. https://doi.org/10.1371/journal.pcbi.1000644.
79. Jorgensen, W.L., Chandrasekhar, J., Madura, J.D., Impey, R.W., and Klein, M.L. (1983). Comparison of simple potential functions for simulating liquid water. J. Chem. Phys. *79*, 926–935. https://doi.org/10.1063/1.445869.
80. Bekker, H., Berendsen, H., Dijkstra, E.J., Achterop, S., Drunen, R., van der Spoel, D., Sijbers, A., Keegstra, H., Reitsma, B., and Renardus, M.K.R. (1993). Gromacs: a parallel computer for molecular dynamics simulations. Phys. Comput. *92*, 252–256.
81. Huang, J., Rauscher, S., Nawrocki, G., Ran, T., Feig, M., de Groot, B.L., Grubmüller, H., and MacKerell, A.D., Jr. (2017). CHARMM36m: an improved force field for folded and intrinsically disordered proteins. Nat. Methods *14*, 71–73. https://doi.org/10.1038/nmeth.4067.
82. Berendsen, H.J.C., Postma, J.P.M., van Gunsteren, W.F., DiNola, A., and Haak, J.R. (1984). Molecular dynamics with coupling to an external bath. J. Chem. Phys. *81*, 3684–3690. https://doi.org/10.1063/1.448118.
83. Darden, T., York, D., and Pedersen, L. (1993). Particle mesh Ewald: an N·log(N) method for Ewald sums in large systems. J. Chem. Phys. *98*, 10089–10092. https://doi.org/10.1063/1.464397.
84. Hess, B. (2008). P-LINCS: a parallel linear constraint solver for molecular simulation. J. Chem. Theor. Comput *4*, 116–122. https://doi.org/10.1021/ct700200b.
85. Tyka, M.D., Keedy, D.A., André, I., Dimaio, F., Song, Y., Richardson, D.C., Richardson, J.S., and Baker, D. (2011). Alternate states of proteins revealed by detailed energy landscape mapping. J. Mol. Biol. *405*, 607–618. https://doi.org/10.1016/j.jmb.2010.11.008.

STAR★METHODS

KEY RESOURCES TABLE

REAGENT or RESOURCE	SOURCE	IDENTIFIER
Antibodies		
APC anti-human IgG Fc Antibody	BioLegend	Cat#409306
PE anti-rat IgG2b Antibody	BioLegend	Cat#408214; RRID: AB_2749893
BV421 Mouse Anti-Human CD279 (PD-1)	BD Biosciences	Cat#565935; RRID: AB_11153482
CD357 (AITR/GITR) Monoclonal Antibody (eBioAITR), PE	eBioscience™	Cat#12-5875-42; RRID: AB_2572634
PE/Cyanine7 anti-human CD3 Antibody	BioLegend	Cat#300316; RRID: AB_314052
Alexa Fluor® 488 anti-human CD4 Antibody	BioLegend	Cat#300519; RRID: AB_389311
Alexa Fluor® 700 anti-human CD8a Antibody	BioLegend	Cat#300920; RRID: AB_528885
Brilliant Violet 785™ anti-human CD25 Antibody	BioLegend	Cat#356140; RRID: AB_2750205
Alexa Fluor® 647 anti-mouse/rat/human FOXP3 Antibody	BioLegend	Cat#320014; RRID: AB_439750
Purified NA/LE Mouse Anti-Human CD3	BD Biosciences	Cat#555329; RRID: AB_395736
Purified NA/LE Mouse Anti-Human CD28	BD Biosciences	Cat#555725; RRID: AB_396068
FITC anti-human CD69 Antibody	BioLegend	Cat#310904; RRID: AB_314839
APC Mouse Anti-Human CD25	BD Biosciences	Cat#555434; RRID: AB_398598
Perm Buffer III	BD Biosciences	Cat#558050; RRID: AB_2869118
Phospho-NFkB p65 (Ser529) Antibody, PE	eBioscience™	Cat#12-9863-42; RRID: AB_2572751
Phospho-NF-κB p65 (Ser536) (93H1) Rabbit mAb, PE	Cell Signaling	Cat#5733
Alexa Fluor® 488 anti-mouse CD45 Antibody	BioLegend	Cat#103122; RRID: AB_493531
Alexa Fluor® 700 anti-mouse CD45 Antibody	BioLegend	Cat#103128; RRID: AB_493715
CD8a Monoclonal Antibody (53-6.7), PerCP-Cyanine5.5	eBioscience™	Cat#45-4321-80; RRID: AB_1107004
Brilliant Violet 510™ anti-mouse CD8a Antibody	BioLegend	Cat#100752; RRID: AB_2563057
CD4 Monoclonal Antibody (GK1.5), APC	eBioscience™	Cat#17-0041-81; RRID: AB_469320
BB700 Rat Anti-Mouse CD4	BD Biosciences	Cat#566407; RRID: AB_2744427
Brilliant Violet 785™ anti-mouse CD3 Antibody	BioLegend	Cat#100232; RRID: AB_2562554
PE anti-mouse CD25 Antibody	BioLegend	Cat#102008; RRID: AB_312857
FOXP3 Monoclonal Antibody (FJK-16s), APC	eBioscience™	Cat#17-5773-82; RRID: AB_469457
TruStain FcX™ (anti-mouse CD16/32) Antibody	BioLegend	Cat#101320; RRID: AB_1574975
FITC anti-human/mouse Granzyme B Recombinant Antibody	BioLegend	Cat#372206; RRID: AB_2687030
PE anti-mouse IFN-γ Antibody	BioLegend	Cat#505808; RRID: AB_315402
Brilliant Violet 421™ anti-mouse TNF-α Antibody	BioLegend	Cat#506328; RRID: AB_2562902
Alexa Fluor® 700 anti-mouse CD45 Antibody	BioLegend	Cat#103128; RRID: AB_493715
CD8a Antibody, PerCP-Cyanine5.5	eBioscience™	Cat#45-0081-82; RRID: AB_1107004

(*Continued on next page*)

Continued

REAGENT or RESOURCE	SOURCE	IDENTIFIER
BUV395 Rat Anti-Mouse CD4	BD Biosciences	Cat#740208; RRID: AB_2734761
BUV737 Hamster Anti-Mouse TCR β Chain	BD Biosciences	Cat#612821
PE/Cyanine7 anti-mouse Ly-6G Antibody	BioLegend	Cat#127618; RRID: AB_1877261
V500 Rat Anti-Mouse I-A/I-E	BD Biosciences	Cat#562366; RRID: AB_11153488
Brilliant Violet 785™ anti-mouse/human CD11b Antibody	BioLegend	Cat#101243; RRID: AB_2561373
Brilliant Violet 421™ anti-mouse CD11c Antibody	BioLegend	Cat#117343; RRID: AB_2563099
BV786 Hamster Anti-Mouse CD183	BD Biosciences	Cat#741032; RRID: AB_2740650
PE anti-mouse/human CD45R/B220 Antibody	BioLegend	Cat#103208; RRID: AB_312993
APC anti-mouse CD64 (FcγRI) Antibody	BioLegend	Cat#139306; RRID: AB_11219391
FITC anti-mouse CD16 Antibody	BioLegend	Cat#158008; RRID: AB_2860740
CD32b Monoclonal Antibody (AT130-2), APC	eBioscience™	Cat#17-0321-82; RRID: AB_2573142
Alexa Fluor® 488 anti-mouse CD16.2 (FcγRIV) Antibody	BioLegend	Cat#149524; RRID: AB_2687088
Alexa Fluor® 700 anti-mouse CD45 Antibody	BioLegend	Cat#103128; RRID: AB_493715
Alexa Fluor® 488 anti-mouse CD4 Antibody	BioLegend	Cat#100529; RRID: AB_389303
BV421 Rat Anti-Mouse CD25	BD Biosciences	Cat#564571; RRID: AB_2738849
CD357 (AITR/GITR) Monoclonal Antibody (eBioAITR)	eBioscience™	Cat#25-5875-42; RRID: AB_2573485
Brilliant Violet 785™ anti-mouse CD45 Antibody	BioLegend	Cat#103149; RRID: AB_2564590
BUV395 Rat Anti-Mouse CD4	BD Biosciences	Cat#740208; RRID: AB_2734761
InVivoMAb anti-mouse CD4	Bioxcell	Cat#BE0003-1; RRID: AB_1107636
InVivoMAb anti-mouse CD8β (Lyt 3.2)	Bioxcell	Cat#BE0223; RRID: AB_2687706
Liberase™ TM Research Grade	Roche	Cat#05401127001
DNase I	Sigma-Aldrich	Cat#D5025-375KU
foxp3 fixation/permeabilization kit	eBioscience™	Cat#00-5523-00
Chemicals, peptides, and recombinant proteins		
Human GITR	ACROBiosystems	Cat#GIR-H5228
Puromycin	Gibco	Cat#A11138-02
Staphylococcal enterotoxin B	TOXIN TECHNOLOGY	Cat#BT202
Brefeldin A Solution	BioLegend	Cat#420601
Alexa Fluor™ 488 Antibody Labeling Kit	Thermo Fisher	Cat#A20181
Alexa Fluor™ 647 Antibody Labeling Kit	Thermo Fisher	Cat#A20186
Bio-Glo™ Luciferase Assay System	Promega	Cat#G7940
Human IFN gamma kit HTRF	Cisbio	Cat#62HIFNGPEG
MILLIPLEX MAP Human High Sensitivity T cell Panel	Millipore	Cat#HSTCMAG-28SK
EasySep™ Human CD4+ T cell Enrichment Kit	STEMCELL	Cat#19052
Human IL2 kit HTRF	Cisbio	Cat#62HIL02PEG
LIVE/DEAD™ Fixable Yellow Dead Cell Stain Kit	Thermo Fisher	Cat#L34968
LIVE/DEAD™ Fixable Near-IR Dead Cell Stain Kit	Thermo Fisher	Cat#L34976

(*Continued on next page*)

Continued

REAGENT or RESOURCE	SOURCE	IDENTIFIER
Deposited data		
ArrayExpress database	EMBL-EBI	E-MTAB-8107
Gene Expression Omnibus (GEO) database	NCBI	GSE123814
Protein Structure	Wang, F et al	PDBID: 7KHD
Experimental models: Cell lines		
HEK293T	ATCC	Cat#CRL-3216
MC38	Obiosh	Cat#HYC3401
B16F10	ATCC	Cat#CRL-6475
CT26	ATCC	Cat#CRL-2638
CHO-S	Invitrogen	Cat#R80007
CTLL-2	ATCC	Cat#TIB-214
Raji	COBIOER	Cat#CBP60272
Jurkat	genomeditech	Cat#GM-C01459
Experimental models: Organisms/strains		
Mouse: C57BL/6-Pdcd1$^{tm1(PDCD1)}$Tnfrsf18$^{tm1(TNFRSF18)}$/Bcgen	Biocytogen	Cat#120528
Mouse: BALB/c-hPD1/hGITR	Gempharmatech	Cat#T004061
Software and algorithms		
ImageJ	Schneider et al., 2012	https://imagej.nih.gov/ij/download.html
Pannoromic MIDI imaging system	3D HISTECH	https://www.3dhistech.com/
HALO® image analysis platform	Indica Labs	https://indicalab.com/halo/
Prism 8	GraphPad Software	https://www.graphpad.com/
Seurat v4.0.1	Hao et al., 2021	https://satijalab.org/seurat/
Scanpy v1.7.1	Wolf et al., 2018	https://github.com/theislab/scanpy
SciPy v1.5.2	Virtanen et al., 2020	https://scipy.org/
Gromacs 2019-3	Bekker, H. et al.	http://www.gromacs.org/
ROSETTA suite	RosettaCommons	http://www.rosettacommons.org

RESOURCE AVAILABILITY

Lead contact

Further information and requests for resources and reagents should be directed to the lead contact Kaijie He (kaijie.he@innoventbio.com).

Materials availability

All unique/stable reagents generated in this study are available from the Lead contact with a completed Materials Transfer Agreement.

Data and code availability

CRC scRNA-seq data used in this study are downloaded from the ArrayExpress database at EMBL-EBI: E-MTAB-8107. Annotated BCC scRNAseq data were downloaded from the Gene Expression Omnibus (GEO) : GSE123814.

The code supporting for modeling, molecular dynamics and in-silico mutagenesis and analysis of this study are available within the article and supplemental information. Other data are available from the corresponding authors upon reasonable request.

Any additional information required to reanalyze the data reported in this paper is available from the Lead contact upon request.

EXPERIMENTAL MODEL AND SUBJECT DETAILS

Cell lines

HEK293T cells (ATCC) were cultured in DMEM supplemented with 10% FBS. Jurkat cells (genomeditech), Raji cells (COBIOER), and CTLL-2 cells (ATCC) were cultured in RPMI1640 supplemented with 10% heat-inactivated FBS. MC38 (HYC3401, Obiosh) and B16F10 (ATCC, CRL-6475) cells were cultured in DMEM supplemented with 10% FBS. CT26 (ATCC, CRL-2638) cells were cultured

in RPMI1640 supplemented with 10% FBS. CHO-S cells (Invitrogen) were electroporated with vectors containing human GITR (NCBI ID: NP_004186.1) or cynomolgus GITR (NCBI ID: XP_005545180.1) according to the manufacturer's instructions. All cell lines were maintained at 37°C in a humidified incubator at 5% CO_2.

Animals

4–6 weeks old female hGITR/hPD1 double knocked-in C57BL6 mice (Biocytogen) or hGITR/hPD1 double knocked-in Balb/c mice (Gempharmatech) were maintained under standardized conditions with a 12 h/day light cycle and controlled temperature (20–22°C) and humidity (40–60%). All mice studies were performed according to Regulations for Care and Use of Laboratory Animals at Innovent Biologics and were approved by Innovent's Institutional Animal Care and Use Committee (IACUC). For cynomolgus monkeys studies, same number of male and female monkeys were included into each group. All monkey experiments were approved by IACUC and performed by WestChina-Frontier PharmaTech, according to the regulations of Association for Assessment and Accreditation of Laboratory Animal Care International (AAALAC).

Human PBMCs

Human PBMCs were purchased from Miao Tong Biological Technology and cultured in AIM V Medium CTS. Miao Tong Biological Technology represents and warrants that it has obtained ownership rights with respect to products and that such products were provided to Miao Tong Biological Technology with every donor's informed consent and in compliance with all applicable laws and regulations.

Donor	Gender	Blood type	Age	Height (cm)	Body weight (kg)
1	male	A	26	175	63
2	male	A	19	173	62
3	male	B	32	160	77
4	male	O	28	185	76
5	male	B	18	172	56
6	male	O	27	175	60
7	male	O	30	178	85
8	male	O	33	180	72
9	female	O	24	171	59
10	male	O	29	169	62
11	male	A	34	175	62

METHOD DETAILS

In vitro assays

Protein expression

For GITRL trimer protein, the coding sequences of a his-tag, a coronin trimeric domain, and the GITRL ECD were cloned into pcDNA3.1 expression vector. For GITRL hexamer protein, the coding sequences of a coronin trimeric domain, a Fc domain, and the GITRL ECD were cloned into pcDNA3.1. Proteins were expressed using Expi293 expression system (Thermo Fisher). Cell supernatants were collected at 5–7 days post-transfection, and proteins were purified using Ni-NTA (Qiagen) or protein A affinity chromatography.

Affinity measurement

Affinity of IBI37G5 to human GITR and cynomolgus GITR were measured on a Biacore T200 using HBS-EP+ (Cytiva, BR-1006-69) as the running buffer. Firstly, anti-human Fc IgG (Abcam, Ab97221) was immobilized on the activated flow cells of a CM5 sensor chip (Cytiva, 29-1496-03) at around 10,000 RU. Then, 2 μg/mL IBI37G5 was captured onto the immobilized sensor chip for 30 s. 2-fold serial dilutions (1.25–40 nM) of human GITR (Acro biosystems, GIR-H5228) and cynomolgus GITR (Sino Biological, 90871-C08H) as well as blank running buffer were injected onto the sensor surface for 180 s, and followed a 600-s phase of dissociation. At the end of each cycle, the sensor was regenerated by a 30-s injection of 10 mM glycine pH 1.5 (Cytiva, BR-1003-54). Raw data were processed using a 1:1 binding model using the Biacore T200 evaluation software version 3.1. For IBI37G5's affinity to FcγR, anti-his antibody (Cytiva, 28995056) was immobilized on the CM5 sensor chip at a density of 6,000–8,000 RU. 1 μg/mL poly-histine FcγRs were added onto the immobilized sensor chip for 60s, and IBI37G5 of different IgG subtypes were injected onto the sensor surface. Cross-reactivity of IBI37G5 were analyzed using Octet Red96e (Fortebio). Briefly, IBI37G5 was loaded onto AHC biosensors (Fortebio) at a density of around 1 nm, and 2-fold serial dilutions of GITR from rhesus, canine, mouse and rat were loaded on the biosensors.

After a 180-s association phase, the biosensors were transferred into SD buffer (1x PBS, 0.1% BSA, 0.05% tween-20) for 600 s for dissociation. All the dilutions were prepared in SD buffer, and experiments were performed at 30°C. Binding affinity was calculated using the Octet Data Analysis software (Version 11.0) using 1:1 binding model.

Competitive binding assay

For ligand competition assay using flow cytometry, Jurkat cells overexpressing human GITR were incubated with varying concentrations of IBI37G5 and mixed with 3 nM GITRL-mFc (Sino Biological, 16080-H38H) in 1% BSA/PBS buffer at 4°C for 30 min. After three PBS washes, competition of IBI37G5 was determined by measuring the binding of GITRL-mFc using APC-labeled goat anti-mouse Fc antibody (Biolegend, 405308). To measure the blocking ability of IBI37G5 to GITR/GITRL by SPR, poly-histine-tagged GITR (ACRO biosystems, GITR-H5228) at 100 nM was loaded onto HIS1K biosensors (18–50, Fortebio) and the loaded biosensors were saturated by 100 nM IBI37G5. SD buffer was used as unsaturated control. 100 nM GITRL trimer protein (manufactured in house) was loaded onto the biosensors for competition and the lack of GITRL binding signal after IBI37G5 saturation indicates a blocking effect.

Epitope mapping

Alanine scanning assay was used to map the binding epitope of IBI37G5 to GITR. Briefly, wild-type GITR and mutant GITR were cloned into pcDNA3.1-EGFP and transiently expressed in HEK293T. Cell binding was measured by flow cytometry 48-h post-transfection.

Receptor occupancy assay

PBMC derived $CD4^+$ T cells were activated by Dynabeads CD3/CD28 (Gibco, 11131D) for 4 days. 2×10^5 activated $CD4^+$ T cells were seeded onto 96-well U-bottom plates and incubated with serially-diluted antibodies for 30 min at 4°C. After several rounds of washes with PBS, samples were stained with Alexa Fluor 488 labeled IBI37G5 (IBI37G5 was conjugated using Alexa Fluor™ 488 antibody labeling kit (Thermo Fisher, A20181)), the intensity of the AF488 fluorescence signal was detected to measure GITR receptor availability on $CD4^+$ T cells by flow cytometry. GITR occupancy was calculated as the mean fluorescent intensity (MFI) ratio of test samples in relative to the cells with over-saturated IBI37G5.

Detection of freely exposed Fabs of IBI37G5

3×10^5 PBMCs or Jurkat-GITR reporter cells were seeded onto 96-well plates and incubated with different concentration of IBI37G5 at 4°C for 1 h. Cells were then fixed with 4% fixative solution (Solarbio, P1110). Recombinant GITR protein (Acrobiosystems, GIR-H5228) conjugated with Alexa Fluor 647(Thermo Fisher, A20173)and anti-human IgG-PE (Southern biotech, 2040-09) were used to stain freely exposed IBI37G5 binding sites and cell surface-bound IBI37G5, respectively. Fluorescent signals were detected by flow cytometry.

Antibody internalization assay

1×10^5 Jurkat-GITR reporter cells were incubated with 100 nM Alexa Fluor 488 labeled IBI37G5 or control IgG at 4°C for 1 h to saturate the cell surface expressed GITR. Unbound IBI37G5 was then washed away and cells were incubated at 37°C for 0, 1, 2, 4, 6 or 8 h. APC anti-human IgG Fc (BioLegend, 409306) was then used to detect remaining IBI37G5 on cell surface. The internalization assay of anti-mouse antibody DTA-1 was performed using the same method with CTLL-2 cells and PE anti-rat IgG antibody (Biolegend, 408214) to detect remaining DTA-1 on cell surface. The internalization rate was calculate with the following formula: $[(MFI_{AF488}/MFI_{APC})_{sample} - (MFI_{AF488}/MFI_{APC})0h]/[(MFI_{AF488}/MFI_{APC})_{control\ IgG} - (MFI_{AF488}/MFI_{APC})_{0h}]$.

Lentivirus production and Jurkat reporter cell line generation

Variants of GITR-EGFP were cloned into pLenti-IRES-puro (Shanghai Generay Biotech) to generate stable cell lines. Briefly, lentiviral plasmid and two associated helper plasmids were co-transfected into HEK293T cells using Lipofectamine 3000 (Invitrogen). Virus-containing medium was collected at 48 and 72 h post-transfection, and the virus was concentrated by Lenti-X™ Concentrator (Clontech, 631231). GITR-AA, GITR-DD, GITR-RR mutant plasmids were constructed as previously described (Wang et al., 2021). Briefly, two phenylalanine residues in hGITR CRD3, F137 and F139, were mutated to alanine (GITR-AA), aspartic acid (GITR-DD), or arginine (GITR-RR), to abolish the hydrophobic receptor-receptor membrane-proximal interface. To construct the chimeric receptor (GITR-41BB), GITR CRD3 region (131–155) was replaced with 41BB CRD4 (136–160). Viral supernatant was transduced into NF-κB reporter Jurkat cell line and selected by EGFP cell sorting and 1 μg/mL puromycin (Gibco, A11138-02).

NF-κB luciferase reporter assay

GITR luciferase reporter Jurkat cells were incubated with anti-GITR Ab or GITRL, together with 3×10^4 Raji cells as the Fc cross-linker at 2:1 ratio, for 6 h at 37°C with 5% CO_2. Luciferase signal was measured using Bio-Glo™ Luciferase Assay System (Promega, G7940) on the SpectraMax i3x plate reader (Molecular Devices).

Expression profile of PD1 and GITR in human T cells

To measure PD1 and GITR expression in activated human T cells, PBMCs (PB100C-W, Miao Tong Biological Technology) were activated with Staphylococcal enterotoxin B (SEB) and flow cytometry was performed at different time points. The antibodies used were anti-PD1 (BD, 562516), GITR (ebioscience, 12-5875-42), CD3 (Biolegend, 300316), CD4 (Biolegend, 300519), CD25 (Biolegend, 356140), CD8 (Biolegend, 300920) and FoxP3 (Biolegend, 320014).

PBMC cytokine release assay

To measure the synergistic effect between PD1 antibody and IBI37G5, 1×10^5 PBMCs were cultured with Staphylococcal enterotoxin B (SEB) in the absence or presence of IBI37G5 or IBI308 for 72 h. Supernatant IFN-γ levels were measured by Human IFN gamma HTRF kit (Cisbio, 62HIFNGPEG). For multiplex PBMC cytokine release assay, a 96-well plate was coated overnight with

0.01 μg/mL to 300 μg/mL of IBI37G5 at 10-fold dilution at 4°C. On the following day, PBMCs from three different donors were added and cultured for 24 h. Cytokines from supernatant were measured using MILLIPLEX MAP Human High Sensitivity T Cell Panel (Millipore, HSTCMAG-28SK)

$CD4^+$ T cell activation assay

Human $CD4^+$ T cells were isolated from PBMCs using EasySep™ Human $CD4^+$ T Cell Isolation Kit (STEMCELL, 19052). 96-well flat-bottom plates were coated with 0.25 μg/mL anti-CD3 (BD, 555329) and incubated with varying concentration anti-GITR antibody at 37°C for 2 h or overnight at 4°C. On the following day, the plate was washed, and 2×10^4 human $CD4^+$ T cells and 2 μg/mL anti-CD28 antibody (BD, 555725) were added. After 3 days, supernatant IL-2 and IFN-γ were measured using Human IL-2 kit (Cisbio, 62HIL02-PEG) and Human IFN-γ kit (Cisbio, 62HIFNGPEG), respectively. Cell surface activation markers were analyzed by flow cytometry using anti-human CD69 FITC (Biolegend, 310904) and anti-human CD25 APC (BD, 555434).

Assessment of NF-κB phosphorylation

To detect the phosphorylation of NF-κB, Jurkat-GITR reporter cells were incubated with IBI37G5. For human $CD4^+$ T cells, T cells were activated with SEB to express GITR and rest for 2 days before incubating with IBI37G5. After 5 min incubation, cells were immediately put on ice to prevent changes in protein phosphorylation. Subsequently, cells were fixed with 4% Paraformaldehyde (Solarbio, P1110) and permeabilized using Perm Buffer III (BD Biosciences, 558050). Phosphorylation of NF-κB was detected using PE-labeled anti-NFκB antibody clone S529 (Invitrogen, 12-9863-42) or clone S536 (Cell Signaling, 5733S) antibodies.

Confocal imaging analysis

Jurkat cells expressing wild type hGITR-GFP or mutant hGITR-GFP (AA/DD/RR) were cultured in RPMI1640 medium with 10% FBS. To detect receptor clustering, 1×10^6 of Jurkat cells were aliquoted into 96-well plates, and incubated on ice with IgG, IBI37G5 or mvIBI37G5 antibodies at various concentrations for 1 h. Cells were then fixed in 4% paraformaldehyde for 15 min at room temperature. After that, cells were washed with PBS twice and stained with DAPI for 6 min. After staining, cells were washed with PBS and mounted on slides with Pro-Long Gold Antifade Mountant (Thermo Fisher, P36961). 3D images were acquired using Leica SP8 confocal microscope and presented as max projection. ImageJ software (NIH) was used to quantitate staining intensity.

Multiplex immunohistochemical staining

Tissue microarray containing tumoral and peritumoral specimens from colon adenocarcinoma patients was stained using the TSA 7-color kit (Yuanxibio, D110071-50T) according to manufacturer's instruction. Antibodies used include anti-human panCK (Genetech, GM351507), anti-human CD8 (Biolynx, BX50036), anti-human FoxP3 (Abcam, ab20034), anti-human PD-1 (Sinobiological, 10377-MM23), anti-human GITR (Cell Signaling, 68014), anti-human CD4 (Abcam, ab133616) and anti-human DAPI (Thermo Fisher, D1306). The stained TMA slide was scanned using Pannoromic MIDI imaging system (3D HISTECH). Number of target cells were counted by HALO Software (Indica Labs).

In silico analysis

scRNAseq analysis

For CRC scRNA-seq, data were obtained from the ArrayExpress database at EMBL-EBI: E-MTAB-8107.[26] All analyses were performed using Seurat 4.0.1,[70] Scanpy 1.7.1[71] and SciPy 1.5.2.[72] Matrices were filtered by removing cells with <201 expressed genes, > 6,000 expressed genes or >25% mitochondrial RNA content. Raw UMI counts were log-normalized. TCR and immunoglobulin genes were removed to avoid clustering based on variable V(D)J transcripts. Confounding factors were minimized by regressing out the number of UMIs, mitochondrial percentage, S phase score, G2/M phase score and heat-shock score. Scaled z-scores were calculated using the ScaleData function. Variable genes were selected using the FindVariableFeatures function, and were used to construct principle components (PCs). PCs were selected based on elbow and Jackstraw plots, and clusters were calculated using the FindClusters function with a resolution of 0.5. Differentially expressed genes in each clusters were calculated using the Wilcoxon Rank Sum test. z-scores for Immune cell markers in each cluster were calculated using SciPy and presented as heatmaps.

For analyzing tumor infiltrating T cells, cells from normal adjacent tissue (N = 1,497) were removed. Clusters were annotated based on known markers as indicated in the heat maps in Figures 1D and S1D. "$CD8^+$ Pre-effector" cluster was annotated based on expression of early activation markers (CST7, DUSP2, GZMK)[26,73,74]

For diffusion map and pseudotime analysis, $CD3^+$ T cells matrices were exported to Scanpy. A neighborhood graph was computed using 20 neighbors and the first 50 PCs, and the first three diffusion components were calculated. A randomly selected naïve T cell was chosen as the root cell and pseudotime was computed using the first 3 diffusion components and a minimum group size of 10. For sliding windows analysis, cells were sorted in ascending order according to pseudotime, and simple moving averages (N = 200) were calculated starting from the 200th cells.

For basal cell carcinoma (BCC) scRNA-seq, annotated data were downloaded from the GEO database : GSE123814 and re-analyzed for GITR, PD1 and CD39 expression, and TCR clonality. Diffusion map was computed in Scanpy using 40 neighbors and the first 20 PCs. Violin plots and diffusion maps were plotted using the standard functions in Seurat.

Human GITR and Fv (IBI37G5) modeling

The complete structure of human GITR protein was modeled based on the crystal structure (PDB: 7KHD) by ROSETTA comparative modeling method.[75] Seven pairs of disulfide bonds were used as additional constraints during the comparison modeling. 10,000 models were generated, and the optimal model was picked with lowest total energy and disulfide geometry potential.

The Fv (IBI37G5) structure was modeled using ROSETTA antibody homology modeling application and further optimized conformations of CDR3 by ROSETTA antibody_H3 application.[76] The detailed scripts are provided in the supplementary materials.

Modeling of the hGITR/Fv (HZ37G5) complex

Global docking of human GITR and Fv (IBI37G5) was implemented by ClusPro antibody docking server[77] with four residues constraints. The fours residues (R90, K105, F106, S107) were assumed at the epitope of GITR based on our experimental evidence (Figures 2F, S2E). 27 global docking results were generated and 15 reasonable docking results were manually picked as the initial complexes based on their cluster size and conformational properties. 15 previously picked docking results were locally refined by ROSETTA SnugDock application.[78] Five hundred refined models were generated for each picked docking model. Among the 7,500 locally refined docking results, the top 2,000 docking models were picked up based on their interface energy. The top 2,000 models were clustered to 10 clusters based on interface RMSD by ROSETTA cluster application (https://new.rosettacommons.org/docs/latest/application_documentation/utilities/cluster). 5 complexes with relatively low energy from 5 different clusters were considered as candidates for further validation by analyzing molecular dynamics.

The 5 candidates of GITR and Fv complexes were solvated in a periodic TIP3P dodecahedron water box with 0.15 M NaCl and 15 Å buffer between the protein and box edge.[79] All simulations were performed in 2019-3 version of Gromacs.[80] The system was modeled with Charmm36 force field.[81] The constructed system was first energy minimized for 50,000 steps using the steepest decent methods, and then heated to 310K with a constant box volume (NVT). Restraints were applied to Cα atoms of the protein with a force constant of 1,000 kJ·mol-1·nm-2 for 1 ns. Subsequently, the heated system was coupled accordingly using isotropic Berendsen control with a time constant of 2 ps for 1 ns pressure regulation (NPT).[82] A non-bonded interaction cut-off of 12 Å was employed. Long-range electrostatics were treated with the particle-mesh Ewald (PME) method.[83] Covalent bonds involving hydrogen atoms were constrained with the LINCS algorithm.[84] Eventually the production MD simulations was running under the random initial speed for a total time of 100 ns, with a time step dt = 2 fs and no restraints applied.

In silico mutagenesis (constraint at C-terminal)

To investigate the roles played by the two critical phenylalanine residues (F137 and F139) in GITR homo-dimerization, *in silico* mutagenesis was applied to F137 and F139. These two phenylalanine residues were mutated into alanine (A), arginine (R) and aspartic acid (D) simultaneously by ROSETTA relax application.[85] Additionally, a 6 Å distance constraint was applied to the N termini of two GITRs in a homo-dimeric complex to maintain a reasonable conformation on cell membrane. One thousand models were generated for each mutant. ROSETTA interface analyzer was used to calculated the interface binding energy. The detailed scripts are provided in the supplementary materials.

In vivo studies

In vivo *tumor microenvironment profiling*

Tumor dissected from mice were digested with Liberase (Roche, 05401127001) and DNase I (Sigma, D5025-375KU) for 30 min and washed with cold PBS before filtering through a 70 μm cell strainer (Biologix Group). The following antibodies were used for flow cytometry: anti-mouse CD45 (Biolegend, 103122), anti-mouse CD45 (Biolegend, 103128), anti-mouse CD8 (Invitrogen, 45-0081-80), anti-mouse CD8 (Biolegend, 100752), anti-mouse CD4 (Invitrogen, 17-0041-81), anti-mouse CD4 (BD, 566407), anti-mouse CD3 (Biolegend, 100232), anti-mouse CD25 (Biolegend, 102008), anti-mouse FoxP3 (Invitrogen, 17-5773-82), anti-mouse CD16/32 (Biolegend, 101320), anti-mouse granzyme B (Biolegend, 372206), LIVE/DEAD Fixable Yellow Dead Cell Stain Kit (Thermo Fisher, L34968), anti-mouse IFN-γ (Biolegend, 505807) and anti-mouse TNF-α (Biolegend, 506328). For intracellular TNF-α and IFN-γ staining, tumor-infiltrating lymphocytes were incubated with IFN-γ-stimulated (50 IU/mL; 48 h) MC38 cells for 6 h at 37°C in the presence of brefeldin A (Biolegend, 420601), and then TNF-α and IFN-γ were stained with foxp3 fixation/permeabilization kit according to the manufacturers' instructions (eBioscience, 00-5523-00) and analyzed by flow cytometry. For detecting FcγR expression in tumor infiltrating immune cells, flow cytometry analysis of single-cell suspensions from blood, spleen, tumor-draining lymph node and tumor was performed using anti-mouse CD45 (Biolegend, 103128), anti-mouse CD8 (eBioscience, 45-0081-82), anti-mouse CD4 (BD, 740208), anti-mouse TCR βchain (BD, 612821), anti-mouse Ly-6G (Biolegend, 127618), anti-mouse I-A/I-E (BD, 562366), anti-mouse CD11b (Biolegend, 101243), anti-mouse CD11c (Biolegend, 117343), anti-mouse NK-1.1 (BD, 741032), anti-mouse B220 (Biolegend, 103208), anti-mouse CD64 (Biolegend, 139306), anti-mouse CD16 (Biolegend, 158008), anti-mouse CD32b (Thermo Fisher, 17-0321-80), anti-mouse CD16.2 (Biolegend, 149524) and LIVE/DEAD Fixable Near-IR Dead Cell Stain Kit (Thermo Fisher, L34976). To verify the depletion efficiency in CD4 and CD8 immune cells depletion experiment, tumor infiltrated lymphocytes were stained with anti-mouse CD45 (Biolegend, 103149), anti-mouse CD4 (BD, 740208), anti-mouse CD8 (eBioscience, 45-0081-80), anti-mouse CD25 (Biolegend, 102008), anti-mouse Foxp3 (eBioscience, 17-5773-82) and LIVE/DEAD Fixable Near-IR Dead Cell Stain Kit (Thermo Fisher, L34976).

To evaluate the expression of human GITR on tumors and spleen after antibody treatment, the single-cell suspensions from tumors and spleen were stained with the following antibodies: anti-mouse CD45 (Biolegend, 103128), anti-mouse TCR βchain (BD, 612821), anti-mouse CD8 (Invitrogen, 45-0081-82), anti-mouse CD4 (Biolegend, 100529), anti-mouse CD25 (BD, 564571), anti-human GITR (Invitrogen, 25-5875-42), anti-mouse FoxP3 (Biolegend, 320014), LIVE/DEAD Fixable Near-IR Dead Cell Stain Kit (Invitrogen, L34976).

In vivo *efficacy and pharmacokinetics of IBI37G5 in mice*

To evaluate the anti-tumor activity of IBI37G5 *in vivo*, MC38 (HYC3401, Obiosh), CT26 (CRL-2638, ATCC) and B16F10 (CRL-6475, ATCC) were implanted in hGITR/hPD1 double knocked-in C57BL6 mice (Biocytogen) or hGITR/hPD1 double knocked-in Balb/c mice (Gempharmatech). When tumor volume reached 60–100 mm^3, mice were randomly grouped and intraperitoneally injected with

indicated drugs twice per week for 2 weeks. For CD4 and CD8 immune cells depletion experiment, MC38 syngeneic model was used here and when tumor volume reached 60–100 mm^3, mice were randomly grouped and CD4 depletion antibody (Bioxcell, BE0003-1) and CD8 depletion antibody (Bioxcell, AB_2687706) were intraperitoneally injected twice per week for 2 weeks. Anti-PD1 antibody (IBI308) and anti-GITR antibody (IBI37G5) were injected 1 day after the depletion antibody injection. Body weight, maximum length of the major axis (L), and maximum length of the minor axis (W) of tumors were measured twice a week. The tumor volume was calculated using the formula: $(width)^2 \times length/2$. Mice were euthanized either when the tumor volume reached 2000 mm^3, or the percentage of body weight loss exceeded 20%.To measure the pharmacokinetics (PK) profiles of IBI37G5, mice were injected intravenously with a single dose of 0.3, 1, 3, or 10 mg/kg of IBI37G5. Blood samples for PK analysis were collected at pre-treatment, and 0.083, 0.5, 2, 6, 24, 48, 96 and 168 h post-treatment for PK analysis. The plasma concentration of IBI37G5 was determined by ELISA

Pharmacokinetics and toxicity study of IBI37G5 in cynomolgus macaques

In a single-dose pharmacokinetic (PK) experiment, 18 cynomolgus monkeys (three per sex per group) received a single dose of IBI37G5 intravenously at 1, 3, or 10 mg/kg. Blood samples for PK analysis were collected pre-treatment, and 0.017, 1, 2, 4, 8, 24, 72, 120, 168, 240, 336, 504, 672, 840, and 1008 h post-dose. The plasma concentration of IBI37G5 was determined by ELISA.

For toxicity study, 40 cynomolgus monkeys (five per sex per group) were intravenously injected with 8 doses of IBI37G5 at 0, 10, 30 or 100 mg/kg once every fortnight for a total of 14 weeks. Lymphocytes subsets were analyzed using flow cytometry at pre-treatment, 1 day after the 3^{rd} dose, 1 day after the 8^{th} dose, and week 25 (the recovery phase). Cytokines (IFN-γ, TNF-α, IL-2, IL-6, IL-8, IL-10) in plasma were measured at pre-treatment, 2 and 24 h after 1^{st}, the 3^{rd}, and the 8^{th} dose. Organs, including thymus and adrenal gland, were collected for hematoxylin and eosin staining after euthanasia.

QUANTIFICATION AND STATISTICAL ANALYSIS

Linear regression module was used for correlation analysis. Ordinary one-way ANOVA or unpaired Student's t tests were used for comparisons between groups. two-way ANOVA and Turkey's multiple comparison tests were used to assess continuous variables.